

Inverse Rendering for Tomographic Volumetric Additive Manufacturing

BAPTISTE NICOLET*, École Polytechnique Fédérale de Lausanne (EPFL), Switzerland

FELIX WECHSLER*, École Polytechnique Fédérale de Lausanne (EPFL), Switzerland

JORGE MADRID-WOLFF, École Polytechnique Fédérale de Lausanne (EPFL), Switzerland

CHRISTOPHE MOSER, École Polytechnique Fédérale de Lausanne (EPFL), Switzerland

WENZEL JAKOB, École Polytechnique Fédérale de Lausanne (EPFL), Switzerland

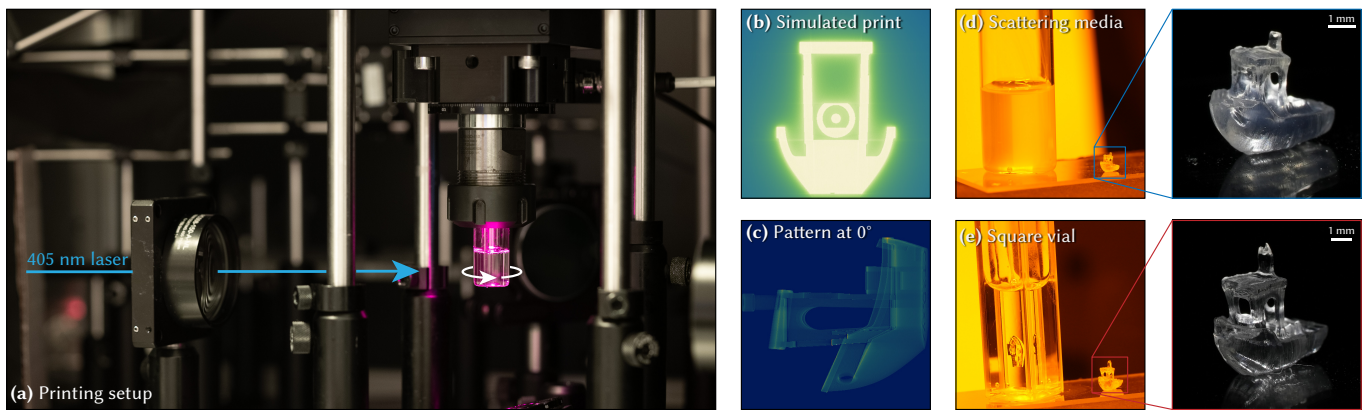


Fig. 1. (a) Tomographic Volumetric Additive Manufacturing fabricates objects by projecting light patterns onto a rotating vial of photo-sensitive resin. We introduce a differentiable rendering framework that (b) can simulate scattering of light in arbitrary resins and (c) compute appropriate patterns for fabrication. Our method enables several applications, such as (d) printing in scattering resins or (e) unusual geometries such as square vials.

Tomographic Volumetric Additive Manufacturing (TVAM) is an emerging 3D printing technology that can create complex objects in under a minute. The key idea is to project intense light patterns onto a rotating vial of photo-sensitive resin, causing polymerization where the cumulative dose of these patterns reaches the polymerization threshold. We formulate the pattern calculation as an inverse light transport problem and solve it via physically based differentiable rendering. In doing so, we address long-standing limitations of prior work by accurately modeling and correcting for scattering in composite resins, printing in non-symmetric vials, and supporting unusual printing geometries. We also introduce an improved discretization scheme that exploits the ray tracing operation to mitigate resolution-related artifacts in prints. We demonstrate the benefits of our method in real-world experiments, where our computed patterns produce prints with an improved fidelity.

*Both authors contributed equally to this work.

Authors' Contact Information: Baptiste Nicolet, École Polytechnique Fédérale de Lausanne (EPFL), Switzerland, baptiste.nicolet@epfl.ch; Felix Wechsler, École Polytechnique Fédérale de Lausanne (EPFL), Switzerland, felix.wechsler@epfl.ch; Jorge Madrid-Wolff, École Polytechnique Fédérale de Lausanne (EPFL), Switzerland, jorge.madridwolff@epfl.ch; Christophe Moser, École Polytechnique Fédérale de Lausanne (EPFL), Switzerland, christophe.moser@epfl.ch; Wenzel Jakob, École Polytechnique Fédérale de Lausanne (EPFL), Switzerland, wenzel.jakob@epfl.ch.

Permission to make digital or hard copies of all or part of this work for personal or classroom use is granted without fee provided that copies are not made or distributed for profit or commercial advantage and that copies bear this notice and the full citation on the first page. Copyrights for components of this work owned by others than the author(s) must be honored. Abstracting with credit is permitted. To copy otherwise, or republish, to post on servers or to redistribute to lists, requires prior specific permission and/or a fee. Request permissions from permissions@acm.org.

© 2024 Copyright held by the owner/author(s). Publication rights licensed to ACM. ACM 1557-7368/2024/12-ART228
<https://doi.org/10.1145/3687924>

CCS Concepts: • Computing methodologies → Rendering; • Applied computing → Physics.

Additional Key Words and Phrases: Inverse rendering, differentiable rendering, additive manufacturing, scattering

ACM Reference Format:

Baptiste Nicolet, Felix Wechsler, Jorge Madrid-Wolff, Christophe Moser, and Wenzel Jakob. 2024. Inverse Rendering for Tomographic Volumetric Additive Manufacturing. *ACM Trans. Graph.* 43, 6, Article 228 (December 2024), 17 pages. <https://doi.org/10.1145/3687924>

1 INTRODUCTION

Tomographic Volumetric Additive Manufacturing (TVAM) [Kelly et al. 2019; Bernal et al. 2019; Loterie et al. 2020] is a recent additive manufacturing technology that enables rapid fabrication of centimeter-scale objects by projecting spatially and temporally modulated illumination patterns onto a rotating vial of translucent photo-sensitive resin (Figure 2a). Well-designed patterns superimpose incoherently in such a way as to overcome a polymerization threshold only in the desired parts of the volume.

In contrast to traditional vat additive manufacturing technologies that print layer by layer (e.g., DLP [Tumbleston et al. 2015] and SLA [Kodama 1981; Hull 1996]) TVAM fabricates the entire object at once, shortening the process to few seconds. The resin furthermore holds the object in place, removing the need for support structures.

To obtain high-quality parts, we generally seek patterns such that their cumulative dose is maximized in the region of interest and minimized elsewhere, which can be formulated as a numerical optimization problem.

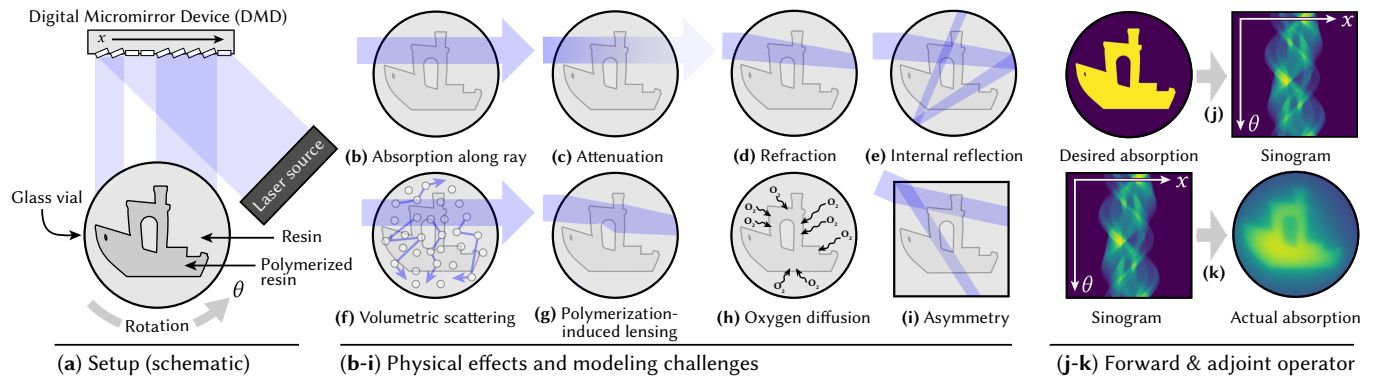


Fig. 2. (a) We consider a tomographic volumetric additive manufacturing (TVAM) setup that exposes a volume of light-sensitive resin to structured illumination patterns from multiple angles. (b) Absorption of the incident beam by a photoinitiator generates polymerization-inducing *free radicals* that are first scavenged by dissolved oxygen (or other inhibitors). Polymerization begins once enough inhibitor has been depleted. In reality, this process involves a number of additional problems: (c) Volumetric attenuation reduces the flux at distant parts of the volume. (d) Changes in the refractive index impact the angle and energy of the transmitted beam. (e) Specular reflections within the vial indirectly expose the resin from other angles. (f) Volumetric scattering diffuses light through the entire vial, causing unwanted polymerization elsewhere. (g) Polymerized regions possess a different refractive index than unpolymerized regions, causing ray bending and self focusing. (h) Oxygen molecules migrate to depleted regions, further inhibiting polymerization and introducing a time dependency in the printing process. (i) Unusual geometries can lead to complex light paths. (j) Given an input 3D model, it is relatively straightforward to create a *sinogram* that integrates the desired absorption along emission rays. (k) However, directly using this sinogram as emission pattern produces poor results, since it neither consider the effects described in (b-i), nor how patterns from different views superimpose. We instead formulate the pattern computation as an inverse rendering problem. We do not model time-dependent effects (g, h), but believe our framework is compatible with them.

Previous TVAM systems rely on the (attenuated) Radon transform and its adjoint operator, referred to as *backprojection*. A simple algorithm to calculate projection patterns is the positive constrained *filtered backprojection* (FBP), which can be further enhanced by iterative approaches. However, the Radon transform represents a simplified physical model lacking various effects that affect the printing process (Figure 2, b-i). In particular, this framework can not account for scattering by particles within the resin.

The ability to correct for scattering is especially important when TVAM is used in composite media, such as biomaterials with living cells [Bernal et al. 2019]. In this case, the printer polymerizes a bio-compatible gel containing cells that scatter a portion of the incident illumination. Prior work approximated scattering as a uniform spatial convolution, using deconvolution to modify the absorption volume [Madrid-Wolff et al. 2022].

Instead we formulate the TVAM pattern computation as a physically based inverse rendering problem, using a differentiable simulation of light within an arbitrary scattering or absorptive volume. Besides improved fidelity compared to the previous method, our approach brings additional flexibility: in prior work, the ability to model the physical setup via backprojection posed a severe constraint requiring specific printing geometries, collimated lighting, or index-matching baths. The proposed method performs gradient-based inversion within an essentially arbitrary configuration and can adapt to whatever is convenient to build and use in practice.

While designing our method, we observed that common TVAM optimization objectives are highly sensitive to the volume resolution and cause aliasing artifacts in prints. We incorporate information about the non-voxelized target surface during the optimization, enabling recovery of sub-voxel details.

Our contributions are:

- A differentiable volumetric rendering formulation of the TVAM process in arbitrary resins.
- An improved discretization of the integration volume that allows to recover details smaller than the voxel size.
- A general optimization framework that can accommodate the variety of existing TVAM setups and resins.

While we currently ignore time-dependent effects, we believe our framework could be extended to include them in future work. Our reference implementation can be found at <https://github.com/rgl-epfl/drtvam>.

2 BACKGROUND

The theoretical foundation of TVAM is closely related to computed tomography (CT). A CT device images X-rays following their passage through a patient or physical sample. Rotating both X-ray source and sensor produces a sequence of angular projections that encode the integrated absorption along a set of rays. Computational inversion can then turn this data into cross-sectional images (2D “slices”) describing the X-ray absorption at every point; stacking a set of such slices finally produces a 3D volume.

The inversion step is traditionally based on the Radon transform, which is a linear operator that converts 2D slices into *sinograms* representing the integrated absorption along a set of rays (Figure 2j).

The adjoint of this operator, known as *backprojection*, takes a sinogram as input and then uniformly deposits absorption along the associated set of rays. Chaining the Radon transform and backprojection produces a blurry rendition of the original volume (Figure 2k), which should not be a surprise, as backprojection realizes the adjoint rather than the inverse of the Radon transform.

The characteristics of this undesired blur are, however, well-understood and can be removed using *filtered backprojection*, which convolves the measurements with a ramp filter to compensate for oversampling of low frequencies.

Intuitively, a TVAM printer can be understood as the adjoint of a CT scanner. Instead of measuring projections, it projects patterns using a light modulator, thereby “implementing” the backprojection operator. This illumination is normally assumed to traverse the printing volume along a straight line, while a *photoinitiator* (PI) absorbs a negligible portion to generate *free radicals* (i.e., reactive molecules). They participate in two competing processes: free radicals trigger polymerization of the resin, while dissolved oxygen simultaneously acts as an *inhibitor* that scavenges free radicals.

Consequently, polymerization only begins once the cumulative absorbed radiation at a given position exceeds a certain light dose threshold (J cm^{-3}), such that enough inhibitor is depleted. For example, one can slightly underexpose a print and then illuminate an empty-looking vial with uniform illumination, at which point the object suddenly appears [Rackson et al. 2022].

From a purely mathematical point of view, it would appear that the CT imaging toolbox readily generalizes to TVAM, enabling prints with perfect contrast by polymerizing the target volume uniformly and keeping light out of empty regions. The main flaw with this idea is that filtered backprojection produces patterns with unrealizable negative intensities. In the early days of TVAM, these were simply clipped to zero [Bernal et al. 2019].

However, clipping leads to severe artifacts in prints that more sophisticated modeling can avoid. Similarly, absorption is not negligible in practice, and modeling the associated exponential decay can improve the quality of prints. The next section reviews these and many other improvements pursued by prior work.

3 RELATED WORK

TVAM has been under intense development since its inception in 2019 [Kelly et al. 2019; Bernal et al. 2019; Loterie et al. 2020]. We review key advances developed during this time.

3.1 Tomographic Volumetric Additive Manufacturing

Optimization-based approaches. The Radon transform assumes lossless light propagation, which is only valid for transparent resins containing very low photoinitiator concentrations. The *attenuated* Radon transform [Natterer 2001; Kelly et al. 2019] removes this discrepancy by modeling the absorptive decay of the incident beam.

To constrain the solution to positive-valued patterns and avoid clamping artifacts, Kelly et al. [2019] employed projected gradient descent to minimize the L_2 distance to a binary target dose (i.e., 1 inside the object, 0 outside). This method is highly sensitive to both step size and initialization.

Common 3D printing resins remain liquid until the cumulative absorbed light exceeds a material-dependent dose threshold [Gibson et al. 2015]. This provides a certain degree of flexibility that the optimization can leverage: concretely, some absorption in empty regions is tolerable as long it remains below the polymerization threshold. Rackson et al. [2021] use this insight in an iterative Radon

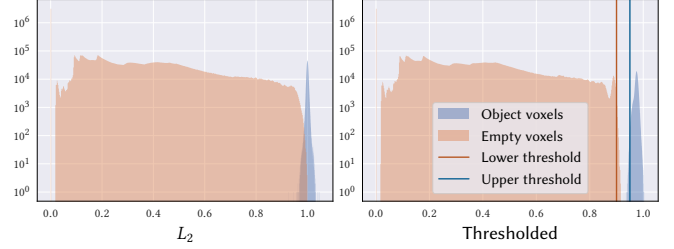


Fig. 3. Histograms of the volumetric absorption following back-projection of the optimized illumination patterns. The two colored regions in each plot distinguish filled and empty regions. A clear separation implies that a perfect print can in principle be achieved by adjusting the light source intensity to reach a polymerization threshold that lies in between. The plots also show that the objective function of Wechsler et al. [2024] (Equation 1) is better-suited to achieve such a separation as compared to a simpler L_2 penalty.

transform-based optimization that replaces the binary target volume with upper (T_U) and lower (T_L) thresholds. Wechsler et al. [2024] realize these constraints in a gradient-based optimization and furthermore penalize *over-polymerization*. This refers to regions receiving an unreasonably high dose so that they polymerize early. This is harmful because the higher refractive index of solidified resin causes undesired lensing of the incident beam (Figure 2g) [Kewitsch and Yariv 1996; Rackson et al. 2022]. To reduce this effect, all parts of the object should appear roughly at the same time [Lotarie et al. 2020]. The thresholded loss of Wechsler et al. [2024], reproduced below, models these goals:

$$\begin{aligned} \mathcal{L} = & \underbrace{\sum_{v \in \text{object}} \text{ReLU}(T_U - I_v)^2}_{\text{force polymerization in object}} + \underbrace{\sum_{v \notin \text{object}} \text{ReLU}(I_v - T_L)^2}_{\text{prevent polymerization elsewhere}} \\ & + \underbrace{\sum_{v \in \text{object}} \text{ReLU}(I_v - 1)^2}_{\text{avoid over-polymerization}}. \end{aligned} \quad (1)$$

Here, I_v denotes the relative light dose in voxel v following back-projection, and T_U and T_L are the upper and lower intensity thresholds. The T_U parameter is generally chosen to be as high as possible to limit over-polymerization. In our experiments, we usually set $T_U = 0.95$ and $T_L = 0.9$.

To check the quality of computed patterns, we can examine the histogram of absorbed energy throughout the volume (Figure 3). If the thresholds T_U and T_L are suitably chosen, this histogram should display a clear separation between empty and filled regions. Assuming that there is no overlap, thresholding the simulated back-projection at an intermediate value will produce a flawless rendition of the target object.

Recently, Li et al. [2024b] used a similar approach to allow for a fractional target dose.

Ray tracing approaches. The first works on TVAM placed the resin vial into a refractive-index matching bath to satisfy the straight ray assumption of the Radon transform. Loterie et al. [2019] and Orth et al. [2021] did away with this inconvenient requirement by

warping the computed patterns to account for refraction at the air-resin interface. This is slightly inaccurate because it ignores changes in the attenuation along the refracted ray segment. Subsequent work [Webber et al. 2023a] introduced a more general ray tracing scheme that handles both refraction and reflection at the air-glass-resin interface. Recently, Li et al. [2024b] simulated spatially varying absorption and curved paths in a gradient index medium, though they did not demonstrate the benefits of this model experimentally.

Deconvolution approaches. The original Radon transform handles clear media, and extensions further account for absorptive decay. However, scattering is beyond the scope of such model. Madrid-Wolff et al. [2022] made the two compatible by interpreting scattering as a uniform spatial convolution that dampens high frequencies. They calculated the Fourier spectrum of this kernel from registered photographs of the material and then deconvolved the computed projections to improve the contrast of prints. We experimentally compare our method to this technique.

Oxygen diffusion (Figure 2h) is another deterioration factor in acrylate-based TVAM. In order to polymerize only parts of the medium, it is important that the material has a nonlinear response to the received light dose so that only parts receiving energy past a given threshold solidify. This behavior is provided by *inhibitors*, such as oxygen for acrylate resins. The price to pay for this thresholded, non-immediate response is that as prints take longer to solidify, oxygen will be depleted in exposed regions and then diffuse from the surroundings to equalize the imbalance in inhibitor concentration, making the necessary light dose difficult to predict. Such modeling inaccuracies cause distortions in prints. This added temporal effect violates the assumption that polymerization at a given position is a function of the local absorption integrated over time [Weisgraber et al. 2023]. Previous works have modeled oxygen diffusion with a time-dependent kernel and similarly deconvolve computed patterns to counteract the induced blur [Orth et al. 2023]. We do not model oxygen diffusion in this work but believe that it could be handled by adding another nested integral to the Monte Carlo sampling process.

Resolution and materials. The resolution of TVAM based printers is currently limited to around $\sim 20\text{ }\mu\text{m}$ [Toombs et al. 2022] for positive features, whereas negative features fare worse [Loterie et al. 2020]. Two wave-optical optimization approaches recently presented simulated results showing that lower feature sizes are optically possible [Wechsler et al. 2024; Li et al. 2024a]. TVAM can print many different materials and objects including optical components, ceramics, glass and biological tissue [Kollep et al. 2022; Toombs et al. 2022; Barbera et al. 2024; Madrid-Wolff et al. 2023; Webber et al. 2024]. Combining TVAM with a conveyor belt geometry may enable high-throughput manufacturing of long structures [Toombs et al. 2024].

Mitigating striation. The last important degradation phenomenon in TVAM is *striation*, which refers to groove-like patterns in generated prints caused by the wave-guiding effects of partially polymerized resin that varies the refractive index [Kewitsch and Yariv 1996]. Removing striation is crucial for parts that require a smooth surface finish, such as optical elements. Rackson et al. [2022]

overcome this problem by only projecting patterns at the beginning of the printing process, followed by a second phase where diffuse illumination uniformly cures resin surpassing an absorptive threshold. Webber et al. [2024] propose an alternative optical system that homogeneously blurs the print to avoid striation at the cost of resolution.

3.2 Physically-based inverse rendering

Our method builds on physically-based inverse rendering and random media.

Inverse rendering. A solution to a wide array of inverse problems in visual computing is the combination of a differentiable image formation model with a gradient-based optimizer. They are typically tasked to recover a virtual 3D scene that is consistent with a set of 2D observations (e.g., photographs taken from different viewpoints). The properties of the forward model are highly application-dependent: for example, differentiable rasterization of triangle meshes [Liu et al. 2019; Laine et al. 2020; Munkberg et al. 2022] produces excellent results when interreflection is not an important effect, or when the reconstruction targets a rendering pipeline with similar constraints (e.g., a computer game based on rasterization). Emissive representations such as *neural radiance fields* [Mildenhall et al. 2020; Müller et al. 2022] or *Gaussian splats* [Kerbl et al. 2023] enable robust and speedy convergence to high-quality representations and have become the method of choice for novel view synthesis.

Physically-based inversion. At the other end are physically-based inverse rendering methods that differentiate a comprehensive Monte Carlo simulation with respect to parameters of the input scene including the material properties of volumes [Gkioulekas et al. 2013, 2016], surfaces [Azinovic et al. 2019], or the geometry itself [Li et al. 2018; Zhang et al. 2020]. One issue underlying all of these methods is that the gradient computation requires access to intermediate steps of the calculation, which must therefore be stored, and this can lead to prohibitive storage costs. Several recent works propose specialized *adjoints* for surfaces/volumes [Nimier-David et al. 2020; Vicini et al. 2021] or gradient-index materials [Teh et al. 2022] that exploit symmetries to eliminate these storage overheads. Differentiable rendering algorithms can be surprisingly difficult to implement on top of standard programming languages and optimization frameworks, which has motivated the development of specialized systems and compilers [Nimier-David et al. 2019; Jakob et al. 2022; Bangaru et al. 2023; Hu et al. 2019].

Radiative transport. Most volumetric modeling in computer graphics relies on the theory of scalar radiative transfer [Chandrasekhar 1960], which describes a statistical distribution of particles that scatter and absorb a portion of the illumination passing through a region of space. In the Monte Carlo context, this requires strategies to randomly sample interactions with particles [Woodcock et al. 1965], and to estimate the *transmittance* (i.e., fractional visibility) along a ray segment [Novák et al. 2014; Kettunen et al. 2021]. Further differentiation-aware sampling strategies may be needed to optimize the density of scattering heterogeneous volumes [Nimier-David et al. 2022].

We assume a properly mixed resin with spatially homogeneous scattering and absorption, which greatly simplifies these steps. In the past, diffusion-based models have been used to approximate volumetric radiative transfer at a lower computational cost [Jensen et al. 2001; Arbree et al. 2011], and these can likewise be inverted [Deng et al. 2022]. In the last years, the field has largely moved away from diffusion-based models, as they produce severe errors when their assumptions¹ are not satisfied. For a more extensive review of volumetric rendering, we refer the reader to Novák et al. [2018].

Fabrication. Physically-based differentiable rendering has been applied in several fields for fabrication.

In the context of inkjet 3D printing, the placement of microscopic ink droplets in an object has a strong influence on its final appearance. Due to the material's translucency, incident light undergoes a multiple scattering process inside the volume that blurs the printed colors. Compensating this effect by optimizing droplet placement has been an active field of research, starting with non-gradient based heuristic methods [Elek et al. 2017], later extended to use manually computed derivatives [Sumin et al. 2019] and, most recently, using a completely differentiable rendering model, usable in an end-to-end gradient-based optimization [Nindel et al. 2021].

In two-photon 3D printing, Auzinger et al. [2018] use an inverse-adjoint wave-optical simulation to generate structural color.

For more traditional, FDM-based 3D printing, differentiable rendering has been used to optimize surface properties of fabricated objects to display interesting images when viewed from a specific angle [Wu et al. 2022; Shen et al. 2023; Perroni-Scharf and Rusinkiewicz 2023]. Recent methods have also been proposed to optimize the appearance of printed objects, e.g. correcting for color shifts after varnishing [Condor et al. 2023], or enforcing stealthiness by minimizing reflections [Tojo et al. 2023].

Finally, differentiable ray racing through a lens system can be used to implement an end-to-end differentiable image formation pipeline enabling co-design of optical system and image reconstruction. This has applications in computational photography, e.g. to design task-specific lens systems [Li et al. 2021; Sun et al. 2021; Wu et al. 2022] or to fabricate novel optical elements to extract richer information from photographs [Shi et al. 2024].

4 INVERSE RENDERING FOR TVAM

The TVAM process differs from standard rendering in that its output is a *volume*, represented as a voxel grid. To optimize the illumination patterns, we therefore need to define a suitable rendering model that produces volumes. This section explains the radiative transfer model, proposes efficient differentiable estimators for volumetric absorption, and shows how to more directly leverage the target geometry during the optimization to improve the resolution of prints. Table 1 lists the notation used throughout this section.

4.1 Radiative transfer model

The radiative transfer equation (RTE) [Chandrasekhar 1960] is the mathematical foundation of volumetric transport in geometric optics. It models radiative gains and losses due to a distribution of

¹Highly scattering media with low scattering anisotropy subject to directionally smooth illumination.

Table 1. Notation used throughout this section.

(\mathbf{x}, ω)	Ray origin and direction
t	Distance along this ray
s	Distance to closest ray-surface intersection
\mathbf{x}	A position in space
\mathbf{x}_t	Ray parameterization $\mathbf{x} + t\omega$
μ_a, μ_s, μ_t	Absorption, scattering, extinction coefficient
\mathcal{S}^2	Unit sphere
$T(\mathbf{a}, \mathbf{b})$	Transmittance between points \mathbf{a} and \mathbf{b}
$f_p(\mathbf{x}, \omega', \omega)$	Phase function
$f_s(\mathbf{x}, \omega', \omega)$	Bidirectional scattering distribution function
$L_i(\mathbf{x}, \omega), W_i(\mathbf{x}, \omega)$	Incident radiance / importance
$L_o(\mathbf{x}, \omega), W_o(\mathbf{x}, \omega)$	Outgoing radiance / importance
$L_s(\mathbf{x}, \omega), W_s(\mathbf{x}, \omega)$	Scattered radiance / importance
$L_e(\mathbf{x}, \omega), W_e(\mathbf{x}, \omega)$	Emitted radiance / importance

absorbing, emissive, and scattering, particles that permeate space. The integral form of this equation is given by

$$L_i(\mathbf{x}, \omega) = \int_0^s T(\mathbf{x}, \mathbf{x}_t) [\mu_a(\mathbf{x}_t) L_e(\mathbf{x}_t, \omega) + \mu_s(\mathbf{x}_t) L_s(\mathbf{x}_t, \omega)] dt + T(\mathbf{x}, \mathbf{x}_s) L_o(\mathbf{x}_s, -\omega), \quad (2)$$

where L_i, L_o, L_e , and L_s denote the incident, outgoing, emitted, and in-scattered radiance on a volumetric *ray space* $\mathbb{R}^3 \times \mathcal{S}^2$. The absorption and scattering coefficients μ_a and μ_s (units of m^{-1}) specify the product of the particles' number density and their respective scattering and absorption cross-sections. The notation $\mathbf{x}_t = \mathbf{x} + t\omega$ parameterizes the ray (\mathbf{x}, ω) , and $s = \inf \{t > 0 \mid \mathbf{x}_t \in \mathcal{A}\}$ gives the distance to the closest ray-surface intersection with surfaces \mathcal{A} , or it equals ∞ when no such intersection exists.

Broadly, the first line of the equation integrates along a ray (\mathbf{x}, ω) to accumulate sources of light (emission, in-scattering). However, only a portion of this radiance will ultimately reach the ray origin \mathbf{x} due to decays along the way (absorption, out-scattering), which the *transmittance* term T models. It is defined as

$$T(\mathbf{x}, \mathbf{x}_q) = \exp \left(- \int_0^q \mu_t(\mathbf{x}_t) dt \right), \quad (3)$$

where $\mu_t = \mu_a + \mu_s$ denotes the *extinction*. The function T maps to $(0, 1]$ and realizes a fractional form of visibility between two points. We use well-mixed resins and treat μ_t as spatially homogeneous, which reduces Equation 3 to the familiar Beer-Lambert law:

$$T(\mathbf{x}, \mathbf{x}_q) = \exp(-\mu_t q) \quad (4)$$

The function L_s referenced by Equation (2) models in-scattered light—that is, light moving through \mathbf{x} along other *other* directions that subsequently scatters so that it now travels along the ray (\mathbf{x}, ω) . The definition of this quantity in terms of a spherical integral

$$L_s(\mathbf{x}, \omega) = \int_{\mathcal{S}^2} L_i(\mathbf{x}, \omega') f_p(\mathbf{x}, \omega', \omega) d\omega' \quad (5)$$

references the *phase function* f_p describing the directional scattering properties of the particles.

Our experiments use sub-wavelength spherical TiO₂ nanoparticles that are governed by Rayleigh scattering at 405nm, which leads

to the following explicit expression for f_p :

$$f_p(\mathbf{x}, \omega', \omega) = \frac{3}{16\pi} (1 + (\omega \cdot \omega')^2) \quad (6)$$

The second line of the RTE (Equation 2) accounts for a distant surface at \mathbf{x}_s (if present), whose outgoing radiance L_o is attenuated by the intermediate volume. This outgoing radiance is composed of surface emission and light scattered by the surface:

$$L_o(\mathbf{x}, \omega) = L_e(\mathbf{x}, \omega) + \int_{S^2} L_i(\mathbf{x}, \omega') f_s(\mathbf{x}, \omega', \omega) |\cos \theta| d\omega', \quad (7)$$

where f_s is the *bidirectional scattering distribution function* (BSDF) of the surface and θ is the angle between the normal and ω' . This equation encodes everything related to surfaces: the optics of the refractive vial, potential optical elements in the beam path, etc.

This completes the explanation of the optical model. Note that while the volume's absorption coefficient is uniform, the actual amount of absorbed power is not. The next subsections develop Monte Carlo estimators to compute this unknown quantity.

4.2 Measurement equation

The RTE models sources and sinks of radiation, but what still remains to be stated is the measurement of volumetric power performed by the forward simulation. We partition the resin volume into voxels V_j ($j = 1, \dots, N$) and define a volumetric "sensor" using an *importance function* W_e with a binary spatio-directional sensitivity (i.e., a box filter).

$$W_e^{(j)}(\mathbf{x}, \omega) = \begin{cases} 1, & \text{if } \mathbf{x} \in V_j, \\ 0, & \text{otherwise.} \end{cases} \quad (8)$$

We use cubic voxels arranged on a regular grid. The absorbed power in voxel j is then given by a product integral involving incident radiance, the absorption coefficient, and importance function over all directions and volume positions:

$$A_j = \int_{\mathbb{R}^3} \int_{S^2} L_i(\mathbf{x}, \omega) \mu_a(\mathbf{x}) W_e^{(j)}(\mathbf{x}, \omega) d\omega dx. \quad (9)$$

In principle, we now have all information needed to implement a Monte Carlo algorithm that recursively samples the measurement equation (9) and referenced integral equations (2, 5, 7) to work its way towards the emitter. However, starting the random walk from the volume is unnecessarily inefficient: first, changes in the refractive index break standard acceleration strategies such as *next event estimation* that would now need to be replaced with specialized and more complex refraction-aware alternatives [Zeltner et al. 2020]. Second, many voxels absorb no or only a small amount of power, and computation spent on them is essentially wasted.

Analogously to Veach's lower-dimensional surface version [Veach 1998, Equation 4.29], we define a volumetric ray-space inner product $\langle \cdot, \cdot \rangle$ to encode an absorption-weighted integral over the volume and sphere. The gist of bidirectional rendering, then, is that this inner product can be evaluated *from either end*, by switching emitted and incident quantities², i.e.:

$$A_j = \langle L_i, W_e^{(j)} \rangle = \langle L_e, W_i^{(j)} \rangle. \quad (10)$$

²For the underlying integration spaces to be truly identical, we can think of the projector as a volumetric emitter, whose volumetric absorption coefficient $\mu_a(t)$ has collapsed onto a plane (i.e., its definition uses a Dirac delta function).

where the latter term references importance-based versions of all previous definitions and equations, such as the following analogous RTE (omitting the superscript j for readability):

$$W_i(\mathbf{x}, \omega) = \int_0^s T(\mathbf{x}, \mathbf{x}_t) [\mu_a(\mathbf{x}_t) W_e(\mathbf{x}_t, \omega) + \mu_s(\mathbf{x}_t) W_s(\mathbf{x}_t, \omega)] dt + T(\mathbf{x}, \mathbf{x}_s) W_o(\mathbf{x}_s, -\omega), \quad (11)$$

This is the approach taken by our forward simulator: we begin by sampling an emitted ray from the laser projector and refract it into the vial. Within the volume, we recursively sample Equation (11), while considering all voxels j simultaneously. This means that one sample can potentially contribute to many parts of the volume, which further increases efficiency. Within one rendering operation, we sample rays from all pixels of all projection angles, resulting in the total dose distribution within the volume.

4.3 Volume accumulators

Analogous to next event estimation in Monte Carlo forward rendering, we split (11) into separate parts involving *emitted importance* W_e and *scattered importance* W_s . The former admits various specializations that we refer to as *accumulators*, since they are responsible for accumulating volumetric contributions.

Simple accumulator. The standard free-flight sampling strategy picks t proportional to $\mu_t(\mathbf{x}_t) T(\mathbf{x}, \mathbf{x}_t)$. The resulting accumulator adds the absorbed portion of light to voxel containing \mathbf{x}_t .

```

1 def accumulate_simple(ray, s, β):
2     t = -log(1 - random()) / μ_t # Free-flight sampling
3     if t < s:
4         x_t = ray(t)
5         j = voxel_index(x_t)
6         tr = exp(-μ_t * t)          # Evaluate the transmittance
7         accumulate(j, tr * μ_a * β) # Accumulate absorption into V_j

```

Here, s refers to the distance to the nearest surface, and β is the importance weight of all previously sampled integrals including emitted radiance (L_e) from Equation (10). The generated distance t can also be reused to sample the scattered importance integral (W_s).

While intuitive and easy to implement, this strategy suffers from severe variance that makes it unusable in practice. It only accumulates into one voxel, and even this often fails when rays escape the resin volume due to its low extinction³. We reproduce it here because it is useful to validate the other accumulators.

Ratio accumulator. To improve efficiency, we must increase the rate of usable samples that fall into the region of interest. We do so by artificially increasing the extinction to a higher value $\bar{\mu}_t \gg \mu_t$ and furthermore accumulating *multiple contributions* along each ray segment, with corresponding weighting changes to ensure that samples remain unbiased. This strategy is reminiscent of *ratio tracking* [Novák et al. 2014] used to render heterogeneous volumes, where $\bar{\mu}_t$ is referred to as the *majorant*. Increasing $\bar{\mu}_t$ decreases variance in exchange for added computation cost.

³The extinction of the resin cannot be *too high*, otherwise light would not be able to reach the center of the vial.

```

1 def accumulate_ratio(ray, s, β):
2     t, tr = 0, 1 # Initial distance and transmittance
3     while True:
4         t -= log(1 - random()) / μt # Take random steps along ray
5         if t >= s: # ... until reaching a surface
6             break
7         xt = ray(t)
8         j = voxel_index(xt)
9         accumulate(j, tr * μa / μt * β)
10        tr *= 1 - μt / μt # Update transmittance

```

Analytic accumulator. As $\bar{\mu}_t \rightarrow \infty$, the previous ratio accumulator performs an increasingly accurate integration of the emission integral, but this eventually becomes unnecessarily inefficient, as the strategy processes the same voxel over and over again.

Considering that the importance $W_e^{(j)}$ is a simple box filter, the amount of light lost to absorption in voxel j is given by an analytic line integral over the filter's support:

$$a_j = L_i \int_{t_0}^{t_1} \mu_a e^{-\mu_t t} dt = L_i \frac{\mu_a}{\mu_t} (e^{-\mu_t t_0} - e^{-\mu_t t_1}) \quad (12)$$

where L_i is the incident radiance at the voxel boundary, and $[t_0, t_1]$ denotes the interval where $x_t \in V_j$. This is similar to *regular tracking* for transmittance estimation [Novák et al. 2018]. We use a *digital differential analyzer* (DDA) [Amanatides et al. 1987] to explicitly step through intersected voxels and accumulate the analytic contribution a_j to the voxel's absorption A_j :

```

1 def accumulate_analytic(ray, s, β):
2     t = 0
3     for j, dt in traverse_dda(ray):
4         t += dt
5         if t >= s:
6             break
7         tr = exp(-μt * t)
8         accumulate(j, μa / μt * tr * (1 - exp(-μt * dt)) * β)

```

Figure 4 illustrates the three different strategies when computing the primal absorption in a scattering resin. The analytic strategy removes all variance from the absorption accumulation, though some variance naturally remains from recursive scattering by particles. This strategy can be slow especially in high-resolution volumes since it must always visit every voxel. The ratio accumulator can be preferable here if some absorption-related noise is tolerable.

Exposure time. Our estimators compute *power*, while polymerization depends on the *energy* received at a given point in space. This missing time factor implies that only the relative scale of the computed absorption matters when assessing the separation of empty and filled resin regions. The absolute scale requires setup-specific calibration, which involves adjusting any of the three following parameters: the intensity of the light source, the rotation speed of the vial during the printing process, or the total number of rotations.

While the absolute scale is irrelevant for the optimization, it is desirable to have the rendering be independent of the grid resolution, hence we record absorption *per volume* (W m^{-3}). This will be critical when deriving our surface-aware discretization (Section 4.4).

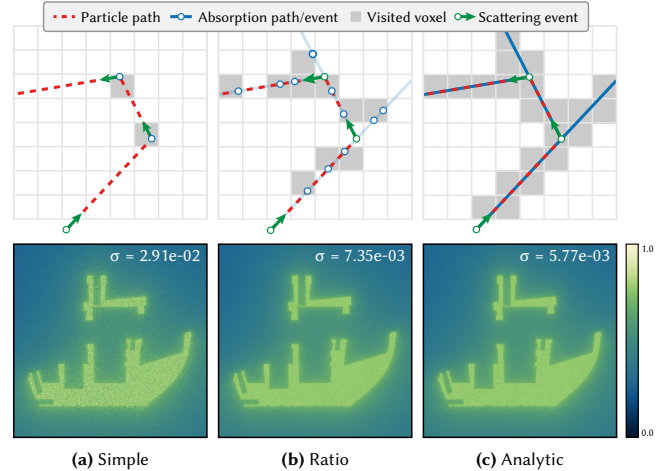


Fig. 4. Evaluation of the three *accumulators* presented in Section 4.3 to estimate the absorption in a scattering resin. (a) Simple free-flight sampling produces unbiased absorption estimates that are, however, too noisy for practical optimization. (b) A variation of ratio tracking exposes a parameter to increase the sampling rate, here using a sampling density more than 200× higher than the medium's extinction. (c) Analytic integration removes all variance related to the accumulation of absorption along rays (that said, some variance remains due to scattering from particles). Each image represents one slice of the computed volume, rendered for 120 s.

Relation to backprojection. Prior works rely on the *backprojection* operator to estimate absorption along a ray. This resembles the DDA traversal of the analytic accumulator except that it sets

$$a_j = L_i \Delta t \quad (13)$$

where $\Delta t = t_1 - t_0$. To address severe errors introduced by the omission of transmittance, the *attenuated* backprojection instead sets

$$a_j = L_i e^{-\mu_t t_i} \Delta t \quad (14)$$

Rewriting Equation (12) using Δt , and using a first-order Taylor expansion when $\mu_t \Delta t \ll 1$, we obtain

$$\begin{aligned} A &= \frac{\mu_a}{\mu_t} L_i e^{-\mu_t t_i} (1 - e^{-\mu_t \Delta t}) \\ &= \mu_a L_i e^{-\mu_t t_i} \Delta t + o((\mu_t \Delta t)^2) \end{aligned} \quad (15)$$

which reveals the attenuated backprojection to be a first-order approximation of our analytic accumulator⁴, when the medium is purely absorptive.

Derivatives. Up to this point, we have only explained the *primal* model. To use it in an actual optimization, we must further differentiate the computed absorption with respect to the input patterns. Efficient implementation of this differentiation step normally requires specialized adjoint integrators [Nimier-David et al. 2020; Vicini et al. 2021]. However, the problem here turns out to be far simpler because we never optimize the optical properties of the medium itself. In fact, Equation (10) implies that the rendering operation is *linear* with regards to the emitted intensities. In this case, the specialized

⁴The μ_a term is not present in Equation (14), so the computed quantities actually differ by a constant factor. This is of no consequence here, as the scale is arbitrary.

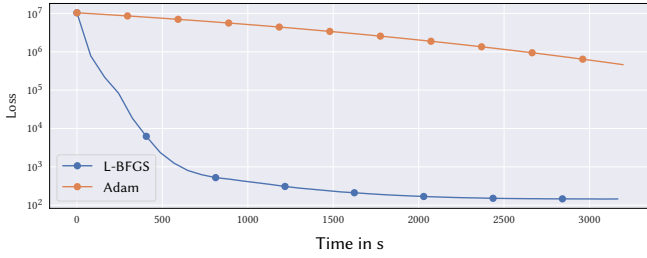


Fig. 5. Equal-time performance comparison using Adam [Kingma and Ba 2014] and L-BFGS [Nocedal 1980]. Each marker denotes 10 iterations. Even though each step with L-BFGS is more expensive than Adam, it converges considerably faster.

adjoints reduce to a simple derivative of the accumulator, which we compute using conventional automatic differentiation [Griewank and Walther 2008].

The linearity of the rendering operation is no panacea: the associated matrix is extremely large, non-sparse, and non-symmetric. However, combined with the convexity of the objective function (Equation 1), it makes this problem suitable for quasi-Newton optimizers and we will therefore use the L-BFGS optimizer [Nocedal 1980].

L-BFGS requires a backtracking line search to find a suitable step size α^* at each iteration:

$$\alpha^* = \arg \min_{\alpha} \mathcal{L}(\mathcal{R}(\mathbf{x} + \alpha \mathbf{p})) \quad (16)$$

Where \mathcal{L} , \mathcal{R} are the loss and rendering functions, respectively, \mathbf{x} is the current state and \mathbf{p} the search direction. This usually entails evaluating an expensive forward model several times at each gradient step. The linearity allows us to rewrite this as:

$$\alpha^* = \arg \min_{\alpha} \mathcal{L}(\mathcal{R}(\mathbf{x}) + \alpha \mathcal{R}(\mathbf{p})) \quad (17)$$

hence only requiring one more rendering call at each step. We note that this performance optimization is specific to our problem, and does not apply to general differentiable rendering tasks.

In the general context of physically-based inverse rendering, we would not expect a quasi-second order method like L-BFGS to perform particularly well, since variance across steps interferes with the optimizer's attempt to build a good Hessian matrix approximation. We can mitigate the effect of this variance using better absorption accumulation strategies (Section 4.3), which makes L-BFGS surprisingly effective. The second-order optimization then only adds a performance overhead of about 38 %, but converges in far fewer iterations than first-order optimizers, as illustrated in Figure 5.

4.4 Improving print resolution using ray tracing

All prior work on TVAM follows essentially the same high-level approach of optimizing absorption values stored on a grid to reach a prescribed goal. Since the target shape is normally a triangle mesh, this requires an intermediate conversion step to turn the mesh into a binary occupancy grid that specifies this goal. The conversion introduces errors that can be significant when the target geometry has sub-resolution features.

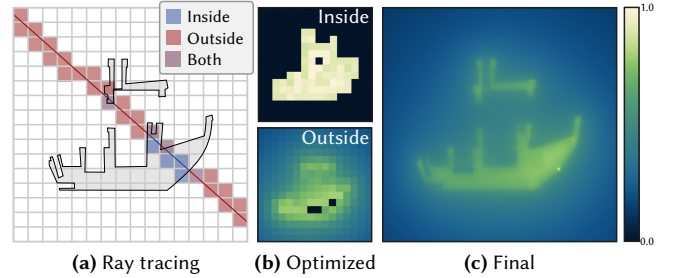


Fig. 6. (a) We show the voxels visited by a given ray in a slice of a 16^3 voxel grid, highlighting voxels receiving a contribution for the inside sub-region, the outside, or both. (b) This splits the rendered volume in two parts. (c) Rendering the final patterns after optimization at a higher resolution (512^3) shows features smaller than the voxel size used during optimization.

Naturally, errors are easily reduced by optimizing with a higher grid resolution, but this increases storage cost and computation time to achieve equally converged results. Alternatively converting the mesh to a *fractional* occupancy grid is also sub-par as it still eliminates information regarding the location of the surface within a voxel. A lossy conversion to an occupancy grid also seems difficult to justify in the rendering context given the ease of computing ray-triangle intersections against high-resolution reference geometry.

Our goal is therefore to more directly incorporate the target geometry in the optimization process, which we do by embedding the unmodified triangle mesh into the virtual scene's resin volume. We continue to partition the volume into voxels V_j , but each voxel is now further split into sub-regions V_j^\bullet and V_j° referring to the parts that fall *inside* and *outside* the target shape (one will typically be empty unless the voxel intersects the surface). We analogously track two separate absorption values A_j^\bullet and A_j° per voxel. The presented method easily generalizes to this representation by selectively accumulating into one of the two with the help of an inside/outside state flag in the random walk that flips when crossing the target surface.

The sub-regions V_j^\bullet and V_j° now represent absorption in regions whose volume can greatly vary. It is therefore crucial to keep track of volumetric absorption that has consistent units, by considering the size of the spatial region over which it is computed. We furthermore compute the fractional volume of the inside/outside region:

$$w_j^\bullet = \text{vol}(V_j^\bullet) / \text{vol}(V_j), \quad \text{and} \quad w_j^\circ = \text{vol}(V_j^\circ) / \text{vol}(V_j) \quad (18)$$

With this added information, we separate the objective into weighted parts considering each region:

$$\mathcal{L} = \sum_j w_j^\bullet \mathcal{L}^\bullet(A_j^\bullet) + w_j^\circ \mathcal{L}^\circ(A_j^\circ). \quad (19)$$

For example, using the thresholded loss [Wechsler et al. 2024]:

$$\begin{aligned} \mathcal{L} = & \sum_j w_j^\bullet [\text{ReLU}(A_j^\bullet - 1)^2 + \text{ReLU}(T_U - A_j^\bullet)^2] \\ & + w_j^\circ \text{ReLU}(A_j^\circ - T_L)^2 \end{aligned} \quad (20)$$

5 RESULTS & DISCUSSION

We explore the use our method to optimize patterns for a variety of TVAM tasks. In doing so, we demonstrate that our method can be used to print in absorptive and scattering media with better fidelity than prior work. We also show that it can correctly account for different vial geometries.

More details about the experimental setup, the materials and protocols used can be found in Appendix A.

In the following, we use the *Intersection over Union* (IoU, also known as Jaccard index) between the target and the simulated printed object as a quality metric. For a given threshold t , it is defined as

$$\text{IoU}(t) = \frac{|P(t) \cap T|}{|P(t) \cup T|}, \quad (21)$$

where $P(t)$ is the set of pixels in the printed object with intensity greater than t and T is the binary target. For each method, we report the maximal IoU achieved for $t \in [0, 1]$.

5.1 Experimental details

Implementation. All experiments in this article were performed on a Linux Ryzen 3990X workstation using a NVIDIA RTX 4090 graphics card. We implemented our method on top of Mitsuba 3 [Jakob et al. 2024] and Dr.Jit [Jakob et al. 2022]. This required to extend Mitsuba to incorporate the accumulation procedures discussed in Sections 4.3 and 4.4 in volumetric sensors, the laser projection model in a new emitter type, and a custom differentiable particle tracer to put these plugins together.

Our printing setup uses collimated lighting, hence we model the projector as a directional area light, though we support other projection models. Unless otherwise specified, we optimize patterns for 1000 angles in the range $[0^\circ, 360^\circ]$ at a resolution of 512^2 pixels for 40 iterations using the L-BFGS optimizer [Nocedal 1980], and the analytic accumulator. The patterns are initialized as zeros, and we use the thresholded loss and a target volume resolution of 512^3 .

The printable volume within the vial is restricted by the area of the emitter being smaller than the vial diameter, and by refractions at the interface. Therefore, recording absorption in the entire vial would be wasteful, as only a fraction of that volume would contain meaningful information. Thus, we restrict our volumetric sensor to the printable region. This is usually done implicitly by methods relying on the Radon transform [Madrid-Wolff et al. 2022].

In our experiments, we observed that pattern pixels where the Radon transform of the target shape is zero have no significant impact on the fabricated object. We therefore added an option to our system to ignore these pixels for ray generation, which accelerated the optimization up to $4.3\times$ in our experiments.

Simulating light transport in a scattering medium is computationally expensive, and depends on the maximum number of simulated scattering events. We find that restricting paths to 3 volume scattering events after entering the vial is sufficient during optimization: it produces results that are indistinguishable from those obtained by simulating more scattering events. When the resin is purely absorptive, we limit path depth to 3. When evaluating the error of the final patterns, we always run the simulation with a maximum path depth of 16.

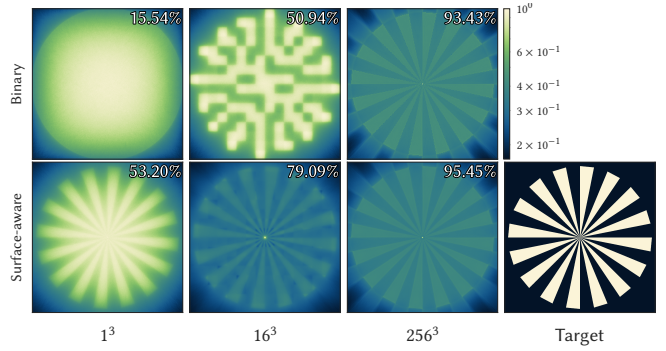


Fig. 7. We optimize patterns for a Siemens star for different discretization resolutions, and render the final state at a higher resolution (1024^3). On each image, we show the best achievable IoU. Binarizing the target geometry introduces severe errors when the target resolution is low. Incorporating the target geometry in the rendering allows to recover more detail at all resolutions.

We observed that the L-BFGS optimizer is quite sensitive to noisy gradients, especially in the first iterations, resulting in high variance in the final patterns. We found that restricting the path depth to 3 (i.e. ignore scattering) for the first 5 iterations was effective in counteracting that noise.

Printing setup. The resin is prepared by mixing an acrylate resin with a photoinitiator⁵. We then measure its absorbance using a spectrophotometer, providing the extinction coefficient μ_t we then use for our optimization.

In all the experiments in this section, unless otherwise stated, we print in a cylindrical vial without an index-matching bath. We usually rotate the vial for 3 or 4 rotations during the exposure time. A single (360°) rotation should in theory be enough to print the object, but partial polymerization towards the end of the print tends to introduce heavy scattering, which can lead to deformations in the final object. Therefore, it is a common practice to rotate the vial multiple times to ensure that the sample is illuminated more uniformly from all angles.

While our rendering is physically-based, it does not replicate every physical detail. The resin polymerization is a complicated physical and chemical process that is sensitive to many parameters, such as oxygen concentration or temperature. Moreover, time-dependent effects (oxygen diffusion, scattering from pre-polymerization, decay of the photo-initiator) also affect the deposited dose. Hence, it is difficult to know the ideal exposure time in advance. To find it, we perform a binary search with respect to the laser power based on whether the obtained print is over- or underpolymerized after visual inspection. After 3 to 5 prints we usually obtain suitable print parameters.

The characteristics of the resin and associated printing parameters for all experiments are summarized in Table 3. For each print, we provide the associated line in that table, e.g. #1 for Figure 8a.

⁵For more information on the materials we used, please see Appendix A.

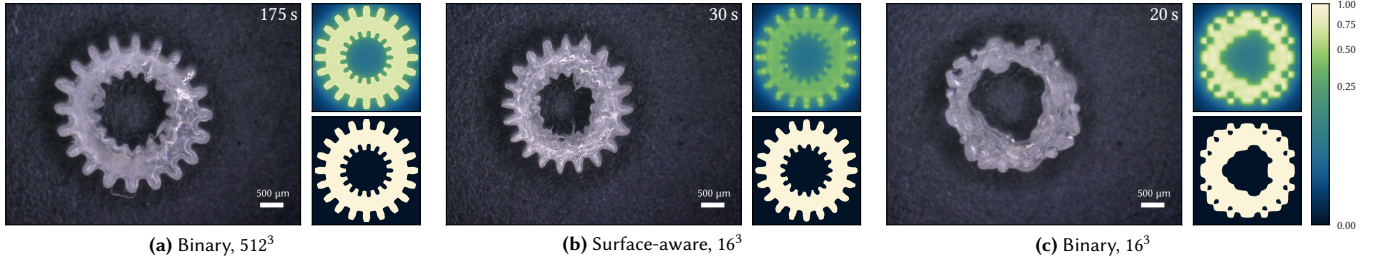


Fig. 8. We print a 4.5 mm diameter gear in a clear resin using three different sets of patterns. For each method, we show a picture of the best print achieved with this set of patterns, and the insets show the simulated dose distribution (top) as well as the simulated print corresponding to the best IoU (bottom). The time written in the top-right corner of each image represents the optimization time for each set of patterns. (a) Using patterns optimized with a 512^3 binary discretization of the target mesh produces a high-fidelity print. (b) Using our surface-aware discretization with a 16^3 resolution still achieves a good print quality, while optimizing considerably faster. (c) Patterns optimized at the same resolution with a binary discretization result in a printed geometry far from the target one, but its shape matches the discretized target well. The printing parameters for (a), (b), (c) are #1, #2, #3 respectively.

5.2 Surface-aware discretization

We first demonstrate the benefits of our surface-aware discretization in simulation and by printing in a clear resin.

Simulation. We optimize patterns for a 3D model of a Siemens star, at various resolutions, using both the binary discretization and our surface-aware discretization. The resolution needed to accurately discretize this object is theoretically infinite, leading to discretization artifacts at all resolutions. We show the results in Figure 7. The binary discretization introduces severe artifacts at low resolutions, and still introduces error at the center of the star at a higher resolution. Our surface-aware discretization allows to recover more detail no matter the resolution.

Surface-aware printing. We validate experimentally the surface-aware discretization mentioned in Section 4.4 by printing a 4.5 mm gear, using three sets of patterns: one optimized for a binary target of a resolution of 512^3 , which represents the best achievable print quality, one using our surface-aware discretization with a target resolution of 16^3 , and one optimized using a binary target of the same resolution. We display the results in Figure 8. Even at such a low resolution, our method achieves a reasonable print quality, for a fraction of the computational cost of the reference. In contrast, merely optimizing with the binary target at the same resolution results in a print that does not resemble the target geometry at all. In all cases, the printed objects are consistent with the simulated dose distribution.

5.3 Advanced geometries

TVAM is still an experimental technology, for which there is no established standard setup. Hence, practitioners have implemented it in a variety of ways. For example, some use a collimated light source (low etendue) while others directly use a LED light source (large etendue). Others use cylindrical vials in an index-matching bath, and some have demonstrated printing without it [Orth et al. 2021; Webber et al. 2023b]. Supporting these various setups is important for the practical applicability of our method, and also enables to experiment with new printing geometries.

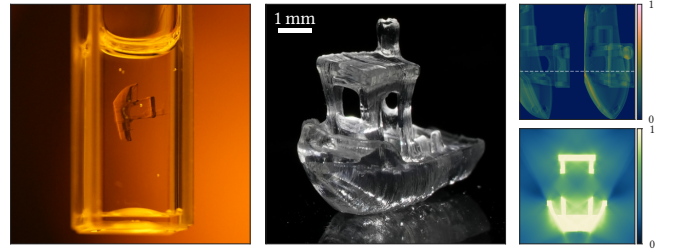


Fig. 9. We illustrate the flexibility of our framework by printing in a square vial (left). The patterns (top right) we optimize account for the strong refraction at the vial’s interface, and produce satisfying results, both in simulation (bottom right) and after fabrication (center). The dashed line in the pattern locates the visualized slice. The printing parameters are #4.

Square vial. We demonstrate this capability by printing objects in a square vial.

On one hand, cylindrical vials are a sound choice for a rotating setup, however these are usually not designed for imaging applications and therefore often have poor optical and manufacturing qualities. In particular, their dimensions can vary significantly (we observe an error of $\pm 80 \mu\text{m}$ in diameter for our round vials). On the other hand, square vials usually have better manufacturing tolerance and optical quality.

We print a 3DBenchy⁶ model in a square vial made of polystyrene and show the results in Figure 9. In simulation, our patterns achieve a perfect reconstruction. The printing parameters are #4.

Note that the vials we use have a rough surface at the corners, which we ignored in our simulation. Our printing setup also does not allow for fine adjustment of the initial orientation of the vial, which is important here, hence it was only approximately positioned. Nevertheless, we achieve a satisfying print quality.

To our knowledge, we are the first to demonstrate such an application. This is promising since it is no longer a hurdle to imagine more complex resin containers for specific applications.

⁶3DBenchy is a popular 3D model used as a benchmark for 3D printing technologies. It is also commonly used in the TVAM literature.

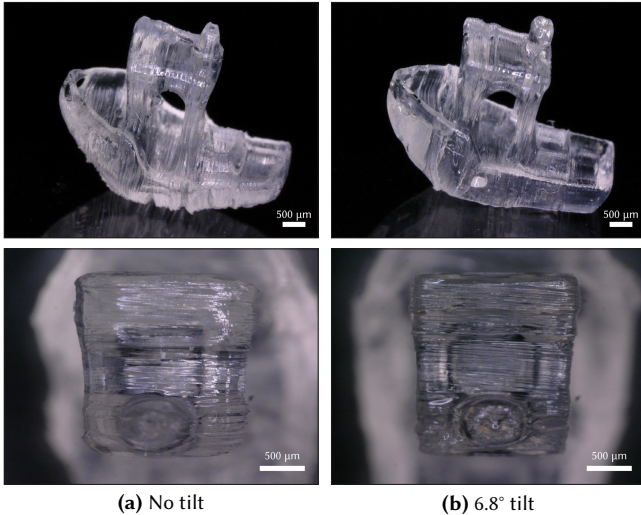


Fig. 10. **(a)** When the rotation axis is perpendicular to the illumination path, the printed object exhibits heavy striations, which can damage it in some regions (see the bottom of the 3DBenchy). **(b)** We tilt the rotation axis of the vial 6.8° towards the light source, a modification for which our method correctly accounts, resulting in a high-fidelity print. Introducing this tilt seems to reduce striations (top), but it does not remove them entirely (bottom). Printing with a higher tilt angle may improve the print quality further. The printing parameters for **(a)** and **(b)** are #5 and #6 respectively.

Tilted rotation axis. We also exploit this flexibility to experiment with the rotation axis of the vial.

Striations are a consequence of self-focusing effects caused by partially polymerized resin on the illumination path [Kewitsch and Yariv 1996]. It is commonly known to affect prints in clear resin, and appears as ripple-like artifacts along the rotation axis in the printed object. In objects printed in scattering media, this effect is less severe. Likewise, horizontal striations are usually not visible.

Based on these observations, we postulate that this is caused by the absence of cross-talk between different horizontal *slices* in the illumination. Indeed, in a clear resin, a single row of the patterns propagates in the same 2D slice. There is only cross talk between the voxels in the same 2D slice but not between adjacent slices. Therefore, defects of self-focusing effects cannot be compensated by different illumination directions.

In order to introduce cross-talk, we propose to tilt the rotation axis towards the light source. In this *tilted geometry*, a single row of a pattern propagates through several adjacent 2D slices. This homogenizes the illumination across several 2D slices and hence reduces striations.

We tilt the rotation axis by 6.8° towards the light source and print a 3DBenchy model in this configuration. We filmed a print in this setup and show it in the supplementary video. We show the resulting print in Figure 10, with printing parameters #5 and #6. Overall, the striations are clearly reduced, especially in the back of the boat. However, they are not completely eliminated. We believe that a higher tilt angle would further improve the print quality, however this remains to be proven experimentally.

Table 2. Relevant metrics for the methods compared in Figure 11. We define the process window Γ as the size of the thresholding window that yields an IoU higher than 95 % of the maximum one achieved by a given method. The pattern efficiency η quantifies the fraction of the total laser output modulated by the DMD. For deconvolution, we report 3 timings: the rendering time for the images used for the deconvolution, the time to compute the deconvolved target, and the optimization time.

Method	\uparrow IoU in %	\uparrow Γ in %	\uparrow η in %	\downarrow T in s
Radon	82.45	4.49	3.25	346
Absorption	85.97	6.29	3.19	346
Deconvolution	93.48	3.60	0.54	1219+198+112
Ours (L_2)	99.31	3.60	3.19	2825
Ours	100.00	6.29	2.80	2825

In simulations, more extreme tilt angles show no degradation in print quality, which supports trying this in future experiments. Note that our simulation does not account for polymerization-induced changes in the refraction index, hence striations are not visible in simulation.

5.4 Simulation of scattering media

We optimize patterns in scattering media and compare simulation results against the following approaches:

- **Radon:** We ignore both attenuation from absorption and scattering in the optimization. In that case, the primal phase of our method reduces to the Radon transform. We convert the target mesh to a binary occupancy grid and use the L_2 error. Even though this method is known to be physically incorrect, it is still common in the literature.
 - **Absorption:** We ignore scattering in the optimization, but we account for attenuation from absorption, assuming that all the extinction comes from it, i.e. $\mu_a = \mu_t$. We use the L_2 loss. This is equivalent to the optimizing using the *attenuated* Radon transform [Kelly et al. 2019].
 - **Deconvolution:** We use the deconvolution method of Madrid-Wolff et al. [2022] to modify the target volume to compensate for scattering. This method requires taking a set of pictures in a specific illumination setup in order to characterize the attenuation of spatial frequencies in the medium of interest. In order to compare it with other methods, we reproduced this capture setup in Mitsuba 3 and used it to render those images for a given medium. We then used the same optimization scheme as described in the paper.
 - **Ours (L_2):** We optimize patterns using our method, under the same L_2 loss used by the methods above.
 - **Ours:** We optimize patterns using our method and the thresholded loss [Wechsler et al. 2024].

The patterns generated from all these approaches are then rendered, with scattering, in our system. We then compute the maximum IoU for each method.

Another important metric is the *process window* [Rackson et al. 2021]. The IoU gives a measure of the maximum achievable quality for a print, but it can be complicated to achieve it. One usually needs to adjust settings such as the laser power or printing time to reach

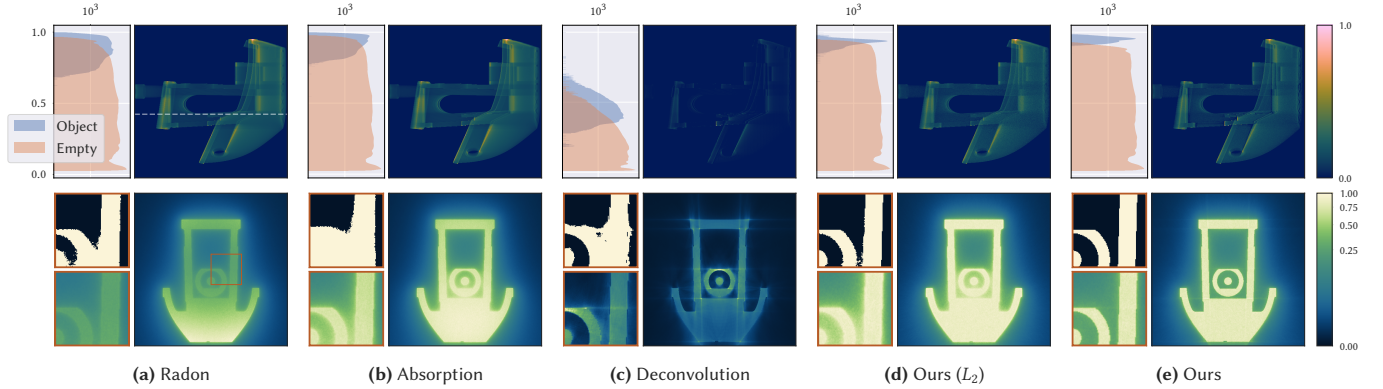


Fig. 11. We optimize patterns for a 3DBenchy in the scattering resin used for Figure 13 with various methods. For each, we show one final pattern (top right), the corresponding dose distribution (bottom right, located by the dashed line) with the histogram of deposited dose (top left). The insets (bottom left) show a zoom on an interesting region of the volume (bottom), and the simulated printed segmentation (top) based on the polymerization threshold achieving the best IoU. (a) Naively optimizing patterns based on the Radon transform leads to a high disparity of absorbed intensity within the target object, resulting in a poor reconstruction. (b) Accounting for attenuation along the ray provides a more uniform dose distribution, but fails to compensate for the blurring introduced by scattering. (c) Deconvolution compensates for attenuation and blurring, but produces very dim patterns with an uneven dose distribution, leading to overpolymerization in some regions. (d) Our method correctly models extinction and scattering in its forward model, producing an even dose distribution in the target area. (e) Our method enables using more advanced objective functions, such as the thresholded loss of Wechsler et al. [2024], which improves contrast between the target region and the background, resulting in a perfect (simulated) print.

the perfect polymerization threshold. The process window gives an idea of how much one can deviate from the optimal settings while still retaining a high quality print. We define the process window as the size of the thresholding window that gives a IoU error higher than 95 % of the maximum one achieved by a given method.

The optimization results can be seen in Figure 11 and the relevant metrics are summarized in Table 2. Deconvolution outperforms the naive baselines, however it produces a narrow process window, as this is not included in the L_2 loss. Our method achieves a higher IoU but also has a narrow process window when using the L_2 loss. When using the thresholded loss we achieve a near perfect simulated print, with a considerably wider process window. This highlights an important benefit of our method: by incorporating scattering directly in the physical model, we are free to choose the objective function, unlike prior work [Madrid-Wolff et al. 2022].

We also found that the deconvolution approach is very sensitive to the initialization and the choice of step size, which has to be tweaked whenever the target object or medium properties would change. In contrast, our method requires no such tuning.

The main drawback of our method is its computational cost. Optimizing with our method is one order of magnitude slower than deconvolution, which is itself an order of magnitude slower than an individual print. However, our method does not require additional data capture before running it, and when accounting for setup time, post-processing, and the need to print a part several times, the optimization time is comparable to the total time required to obtain a finished print.

Influence of scattering on performance. We investigate in Figure 12 how the final error evolves depending on how scattering the medium is. We first fix an extinction coefficient $\mu_t = 0.3 \text{ mm}^{-1}$, and vary the scattering albedo $\alpha = \frac{\mu_s}{\mu_t}$ of the resin.

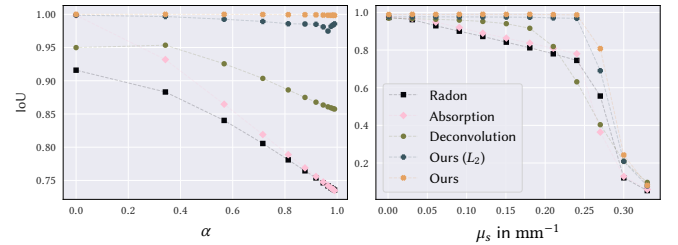


Fig. 12. Evolution of the final error in scattering media. **Left:** we fix the extinction coefficient μ_t and evolve the albedo α . **Right:** We use a fixed absorption and gradually increase the scattering coefficient. Naive methods perform well in the absence of scattering, but degrade quickly. Deconvolution outperforms those methods, but also degrades when scattering increases. In both instances, our method remains stable independently of how scattering the resin is, and only fails when extinction is too high for printing.

Even in the absence of scattering, i.e. $\alpha = 0$, the Radon baseline performs poorly. Indeed, as the extinction is high, not accounting for attenuation along the ray leads to severe errors, which gradually degrade as the medium becomes more scattering. Accounting for absorption improves results initially, but fails when scattering increases. Deconvolution [Madrid-Wolff et al. 2022] improves those methods significantly but still degrades with scattering. In contrast, our method achieves a near-perfect print in all cases. To ensure fair comparison, we also include results using our method with the same objective function as prior works. While it degrades slightly with scattering, it still outperforms the previous methods.

We repeat the same procedure, now varying the scattering coefficient μ_s . Starting from an initially purely absorptive medium ($\mu_t = \mu_a = 0.1 \text{ mm}^{-1}$), we simulate gradually adding scattering particles to the simulation and show how the final error evolves in

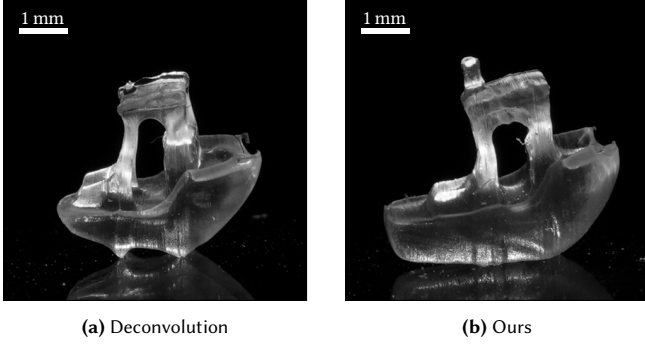


Fig. 13. Printing a 3DBenchy in a scattering resin. (a) The object resulting from deconvolution exhibits underpolymerization in some regions such as the chimney and the back of the boat, while others are overpolymerized, such as the bottom of the boat. We hypothesize that this is caused by oxygen diffusion, as the exposure time needed to print the object is 4.5× longer than with our methods. (b) Our method achieves a higher fidelity print. The printing parameters for (a) and (b) are #7 and #8 respectively.

consequence. In the absence of scattering, i.e. $\mu_s = 0$, all the methods behave similarly. As scattering increases, the naive baselines degrade quickly, while deconvolution and our method remain stable. When extinction is too high, the power required to reach the center of the vial is such that the edge of the vial starts to polymerize first, at which point printing is no longer possible. Our method keeps a high fidelity up to this point, but deconvolution degrades earlier. For certain values of μ_s , deconvolution actually underperforms the naive baselines. For these values, the lack of uniformity in the projected absorption polymerizes a region of the vial away from the object, even though the object region itself has a higher fidelity.

Note that we compare these methods in the absence of an index-matching bath, which differs from the original publication [Madrid-Wolff et al. 2022]. However, we confirm that this does not influence our conclusions in Figure 15.

5.5 Printing in scattering media

We demonstrate that our method can also be used in scattering media.

Characterizing the medium. In order to prepare resins with varying scattering properties, we mix the photo-sensitive resin with TiO₂ nanoparticles, which are known to follow Rayleigh scattering (Equation 6).

We use a spectrophotometer to compute the absorbance of the resin with photoinitiator, before and after introducing the scattering particles. For a general medium, this gives us the following coefficients:

$$\begin{aligned} \mu_{t,1} &= \mu_{a,PI} + \mu_{a,R} \\ \mu_{t,2} &= \mu_t = \mu_{a,PI} + \mu_{a,R} + \mu_{a,S} + \mu_{s,S} \end{aligned} \quad (22)$$

where $\mu_{a,PI}$, $\mu_{a,R}$, $\mu_{a,S}$ are the absorption coefficient of the photoinitiator, resin and scattering particles respectively, and $\mu_{s,S}$ is the scattering coefficient of the scattering particles.

If the albedo α of the scattering particle is known, this is enough to obtain the coefficients of the whole medium⁷:

$$\begin{aligned} \mu_t &= \mu_{t,1} \\ \mu_a &= \mu_{t,1} + \mu_{t,2}(1 - \alpha) \end{aligned} \quad (23)$$

In our case, TiO₂ has no absorption at 405 nm, hence the absorption coefficient is simply the difference between the two measurements. For other media, the albedo and phase function can be estimated from 3 spectral-point measurements [Iser et al. 2022]. This characterization only needs to be done once per scattering particle, and then one can obtain the properties of the resin using the procedure described above. This is a key difference from [Madrid-Wolff et al. 2022], where one would need to capture a set of images every time a resin with a different particle concentration is prepared.

Printing results. We first compare our method against deconvolution [Madrid-Wolff et al. 2022] by printing a 3DBenchy model and a gear in two different scattering resins, whose parameters can be found in Table 3. In both instances, we printed using patterns generated with our method as well as deconvolution [Madrid-Wolff et al. 2022]. For the 3DBenchy, we show the patterns and simulated prints in Figure 11 and a picture of the best print achieved for both methods in Figure 13. The patterns generated by deconvolution are significantly dimmer than ours, which limits the maximum available illumination power. Therefore, we had to expose the vial 4.5× longer before any polymerization occurred. For the printing parameters see #7 for the deconvolution method and #8 for our method. Some of the regions of the resulting print are still underpolymerized, while others are overpolymerized, despite the relatively high quality of the simulated print. We believe this is due to oxygen diffusion: as the printing time increases, more oxygen can flow back to the illuminated regions, thus slowing down polymerization of thinner features of the object, such as the chimney. In comparison, our method achieves a more regular print.

We then printed a 4.5 mm diameter gear in another resin, again using our method and deconvolution method. We show our best achieved print in Figure 14, as well as the three best prints achieved using deconvolution: one that is slightly underpolymerized, one that is slightly overpolymerized, and one in between. We can see that the shape of the over- and under-polymerized objects matches well the prediction from our simulation. This time the printing times are #9, #10, #11, #12 for our method and the three deconvolution method results. Since the printing time is more similar between the two methods, we believe that diffusion is not a main deterioration factor in this case. Our method allows us to get very uniform absorption values inside the object, while the deconvolution method does not, resulting in low fidelity.

Note that Madrid-Wolff et al. [2022] also showed printing results of this gear in their paper, with higher fidelity. However, the gear they printed is more than 2× larger than ours.

⁷The absorption coefficient that we compute here also includes absorption from the resin itself, which does not contribute to polymerization. Absorption from the resin is usually negligible compared to the photo-initiator, but even if it was not, according to Equation (9), this only affects the measurement by a factor of $\frac{\mu_{a,PI}}{\mu_{a,PI} + \mu_{a,R}}$, and the measurement is defined up to exposure time anyway.

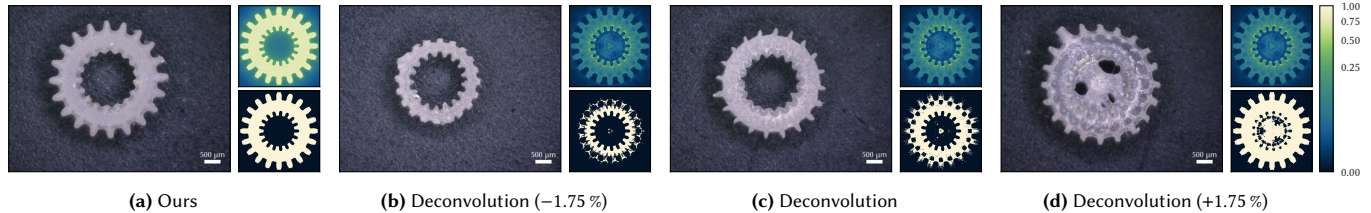


Fig. 14. We print a 4.5 mm diameter gear in a scattering resin, using patterns generated with our method (a) and deconvolution [Madrid-Wolff et al. 2022] (b-d). For each print, we show the simulated dose distribution (top inset) and the thresholded print that best matches the printed object (bottom inset). Deconvolution produces an uneven dose distribution, making it difficult to fabricate the object. (b) Under-exposing by 1.75 % compared to (c) leads to a good reconstruction of the inner cogs, while the outer half of the gear is completely missing. (d) Over-exposing by 1.75 % over-exposure leads to a good reconstruction of the outer cogs, but the inside is over-polymerized. (c) Finding the right exposure level is challenging. The bottom inset shows that the artifacts in (b) and (d) are well predicted by our forward model. (a) In contrast, our method produces a more uniform dose distribution, allowing for higher fidelity prints. The printing parameters for (a), (b), (c), (d) are #9, #10, #11, #12 respectively.

5.6 Discussion

Our inverse renderer shows the importance of accurately modeling the physical processes involved in TVAM in a differentiable way. In the future, we are interested in including more physical effects to improve the quality of our prints.

Most importantly, our method currently does not account for time-dependent effects, which can have a significant impact on the quality of the print. Oxygen diffusion [Orth et al. 2023] affects the printing quality of fine features, especially for long printing times. Including oxygen diffusion in the forward model would allow to optimize the patterns such that its effect is minimized. Pre-polymerized structures scatter and refract light differently than the homogenous resin in the initial state before the print. Also, light reacts with the photoinitiator which reduces its concentration, thus making the medium *heterogeneous*.

All these effects can in principle be simulated with rendering algorithms, therefore an interesting future direction is to include time as an additional integration domain in the measurement equation.

Printing in scattering bio-materials [Bernal et al. 2019, 2022] is promising but also needs to be further investigated. Cells which induce scattering are much larger and less uniform than the TiO_2 particles used in this work, and their properties need to be estimated experimentally, e.g. following Iser et al. [2022].

As demonstrated, tilting the axis of rotation improves the printing quality with respect to striations. We plan on doing further experiments with more extreme tilting angles to investigate this observation in more detail.

Obtaining the best possible print currently requires a manual binary search to find the ideal printing parameters. By having a faithful physical model of the TVAM process, we could use physical units directly in the renderer, which would allow to directly determine the ideal printing parameters such as the exposure time to achieve the best print, thus allowing to forgo this manual process entirely. This is however a challenging endeavor because of all the physical and chemical processes involved. Weisgraber et al. [2023] accurately simulate the polymerization, but this requires expensive computation to solve the related PDEs. The authors report a runtime of 24h on a cluster with 4000 cores to simulate 360s of printing.

Post-processing prints represents an additional challenge to get high-quality prints. The acrylate resins used in TVAM are by design extremely viscous, which makes it difficult to remove all the unpolymerized resin from the printed object, especially in small corners of the object, which can lead to blob-like artifacts in the final object (see for example some of the inner teeth in Figure 8a). Furthermore, the printed object is only partially cured at the end of the printing process, and is therefore relatively soft, which can lead to deformations during post-processing, and even total collapse of some structures. We discuss our strategy to mitigate these defects in Appendix A.4.

Finally, the mathematical formulation of TVAM is related to *inverse treatment planning* [Holmes et al. 1995] in the field of radiotherapy, which entails optimizing the projection of ionizing radiation to concentrate a radiation dose onto malignant tissue in a patient's body. We believe that some elements of our approach could also transfer to such medical applications.

6 CONCLUSION

The quality of projection patterns for Tomographic Volumetric Additive Manufacturing (TVAM) is crucial for superior prints. We demonstrated that framing pattern optimization as an inverse rendering problem can address key limitations of earlier systems. Our versatile physically-based differentiable renderer supports the variety of existing TVAM systems and generate high-quality patterns.

Our method improves printing fidelity in scattering media, which is critical for bioprinting applications. We demonstrate the use of non-standard setups including printing in square vials and a tilted rotation axis for the first time in the literature. The latter improves the undesired striation phenomenon albeit this needs further confirmation. On the computational side, we introduce a surface-aware discretization which reduces resolution-related artifacts in the prints. All results are confirmed in simulation and real-world experiments.

The fully differentiable nature of our method allows for optimization of the printing process and opens up new possibilities for the design of novel TVAM systems. While we currently ignore some physical effects such as oxygen diffusion, our method takes large steps towards accurate differentiable modeling of the physical process of TVAM. We anticipate to include further effects such as diffusion or refractive index changes during printing in the future.

ACKNOWLEDGMENTS

The authors would like to thank the reviewers for their insightful feedback, Sepand Kashani for helpful discussions, Viola Sgarniato for discussions on bio-printing, and Nicolas Roussel and Rami Tabbara for their help with the Mitsuba 3 codebase. 3DBenchy (www.3dbenchy.com) is provided under the CC BY-ND 4.0 license. This project has received funding from the European Research Council (ERC) under the European Union's Horizon 2020 research and innovation program (grant agreement No 948846), and from the Swiss National Science Foundation under project number 196971 - "light based volumetric printing in scattering resins".

Christophe Moser is a shareholder and Jorge Madrid-Wolff is an employee of Readily3D SA. All the other authors declare no conflict of interest.

REFERENCES

- John Amanatides, Andrew Woo, et al. 1987. A fast voxel traversal algorithm for ray tracing.. In *Europgraphics*, Vol. 87. Citeseer, 3–10.
- Adam Arbab, Bruce Walter, and Kavita Bala. 2011. Heterogeneous Subsurface Scattering Using the Finite Element Method. *IEEE Transactions on Visualization and Computer Graphics* 17, 7 (jul 2011), 956–969. <https://doi.org/10.1109/TVCG.2010.117>
- Thomas Auzinger, Wolfgang Heidrich, and Bernd Bickel. 2018. Computational design of nanostructural color for additive manufacturing. *ACM Transactions on Graphics (TOG)* 37, 4 (2018), 1–16.
- Dejan Azinovic, Tzu-Mao Li, Anton Kaplanyan, and Matthias Nießner. 2019. Inverse path tracing for joint material and lighting estimation. In *Proceedings of the IEEE/CVF Conference on Computer Vision and Pattern Recognition*. 2447–2456.
- Sai Bangaru, Lifen Wu, Tzu-Mao Li, Jacob Munkberg, Gilbert Bernstein, Jonathan Ragan-Kelley, Fredo Durand, Aaron Lefohn, and Yong He. 2023. SLANG:D: Fast, Modular and Differentiable Shader Programming. *ACM Transactions on Graphics (SIGGRAPH Asia)* 42, 6 (December 2023), 1–28. <https://doi.org/10.1145/3618353>
- Lorenzo Barbera, Jorge Madrid-Wolff, Roberto Emma, Kunal Masania, Antoine Boniface, Damien Loterie, Paul Delrot, Christophe Moser, and André R Studart. 2024. Multimaterial Volumetric Printing of Silica-Based Glasses. *Advanced Materials Technologies* (2024), 2202117.
- Paulina Nuñez Bernal, Manon Bouwmeester, Jorge Madrid-Wolff, Marc Falant, Sammy Florczak, Nuria Ginés Rodríguez, Yang Li, Gabriel Größbacher, Roos-Anne Samsom, Monique van Wolferen, et al. 2022. Volumetric bioprinting of organoids and optically tuned hydrogels to build liver-like metabolic biofactories. *Advanced Materials* 34, 15 (2022), 2110054.
- Paulina Nuñez Bernal, Paul Delrot, Damien Loterie, Yang Li, Jos Malda, Christophe Moser, and Riccardo Levato. 2019. Volumetric bioprinting of complex living-tissue constructs within seconds. *Advanced materials* 31, 42 (2019), 1904209.
- Subrahmanyam Chandrasekhar. 1960. *Radiative transfer*. Dover publications, New York.
- Jorge Condor, Michal Piovarci, Bernd Bickel, and Piotr Didyk. 2023. Gloss-Aware Color Correction for 3D Printing. In *ACM SIGGRAPH 2023 Conference Proceedings*. 1–11.
- Xi Deng, Fujun Luan, Bruce Walter, Kavita Bala, and Steve Marschner. 2022. Reconstructing translucent objects using differentiable rendering. In *ACM SIGGRAPH 2022 Conference Proceedings*. 1–10.
- Oskar Elek, Denis Sumin, Ran Zhang, Tim Weyrich, Karol Myszkowski, Bernd Bickel, Alexander Wilkie, and Jaroslav Krivanek. 2017. Scattering-aware texture reproduction for 3D printing. *ACM Transactions on Graphics* 36, 6 (2017).
- Ian Gibson, David Rosen, Brent Stucker, Ian Gibson, David Rosen, and Brent Stucker. 2015. Vat photopolymerization processes. *Additive manufacturing technologies: 3D printing, rapid prototyping, and direct digital manufacturing* (2015), 63–106.
- Ioannis Gkioulekas, Anat Levin, and Todd Zickler. 2016. An evaluation of computational imaging techniques for heterogeneous inverse scattering. In *Computer Vision–ECCV 2016: 14th European Conference, Amsterdam, The Netherlands, October 11–14, 2016, Proceedings, Part III* 14. Springer, 685–701.
- Ioannis Gkioulekas, Shuang Zhao, Kavita Bala, Todd Zickler, and Anat Levin. 2013. Inverse volume rendering with material dictionaries. *ACM Trans. Graph.* 32, 6, Article 162 (nov 2013), 13 pages. <https://doi.org/10.1145/2508363.2508377>
- Andreas Griewank and Andrea Walther. 2008. *Evaluating derivatives: principles and techniques of algorithmic differentiation*. Vol. 105. SIAM.
- Timothy W. Holmes, T. Rock Mackie, and Paul Reckwerdt. 1995. An iterative filtered backprojection inverse treatment planning algorithm for tomotherapy. *International Journal of Radiation Oncology*Biology*Physics* 32, 4 (1995), 1215–1225. [https://doi.org/10.1016/0360-3016\(94\)00465-W](https://doi.org/10.1016/0360-3016(94)00465-W)
- Yuanming Hu, Luke Anderson, Tzu-Mao Li, Qi Sun, Nathan Carr, Jonathan Ragan-Kelley, and Frédo Durand. 2019. Difftaichi: Differentiable programming for physical simulation. *arXiv preprint arXiv:1910.00935* (2019).
- Charles W Hull. 1996. Apparatus for production of three-dimensional objects by stereolithography. US Patent 5,556,590.
- Tomás Iser, Tobias Rittig, Emilie Nogué, Thomas Klaus Nindel, and Alexander Wilkie. 2022. Affordable spectral measurements of translucent materials. *ACM Transactions on Graphics (TOG)* 41, 6 (2022), 1–13.
- Wenzel Jakob, Sébastien Speirer, Nicolas Roussel, Rami Tabbara, Merlin Nimier-David, Delio Vicini, Tizian Zeltner, Baptiste Nicolet, Miguel Crespo, Vincent Leroy, and Ziyi Zhang. 2024. *Mitsuba 3 renderer*. <https://mitsuba-renderer.org>.
- Wenzel Jakob, Sébastien Speirer, Nicolas Roussel, and Delio Vicini. 2022. DrJit: A Just-In-Time Compiler for Differentiable Rendering. *Transactions on Graphics (Proceedings of SIGGRAPH)* 41, 4 (July 2022). <https://doi.org/10.1145/3528223.3530099>
- Henrik Wann Jensen, Stephen R. Marschner, Marc Levoy, and Pat Hanrahan. 2001. A practical model for subsurface light transport. In *Proceedings of the 28th Annual Conference on Computer Graphics and Interactive Techniques (SIGGRAPH '01)*. Association for Computing Machinery, New York, NY, USA, 511–518. <https://doi.org/10.1145/383259.383319>
- Brett E Kelly, Indrasen Bhattacharya, Hossein Heidari, Maxim Shusteff, Christopher M Spadaccini, and Hayden K Taylor. 2019. Volumetric additive manufacturing via tomographic reconstruction. *Science* 363, 6431 (2019), 1075–1079.
- Bernhard Kerbl, Georgios Kopanas, Thomas Leimkühler, and George Drettakis. 2023. 3d gaussian splatting for real-time radiance field rendering. *ACM Transactions on Graphics* 42, 4 (2023), 1–14.
- Markus Kettunen, Eugene D'Eon, Jacopo Pantaleoni, and Jan Novák. 2021. An unbiased ray-marching transmittance estimator. *ACM Trans. Graph.* 40, 4, Article 137 (jul 2021), 20 pages. <https://doi.org/10.1145/3450626.3459937>
- Anthony S Kewitsch and Amnon Yariv. 1996. Self-focusing and self-trapping of optical beams upon photopolymerization. *Optics Letters* 21, 1 (1996), 24–26.
- Diederik P Kingma and Jimmy Ba. 2014. Adam: A method for stochastic optimization. *arXiv preprint arXiv:1412.6980* (2014).
- Hideo Kodama. 1981. Automatic method for fabricating a three-dimensional plastic model with photo-hardening polymer. *Review of scientific instruments* 52, 11 (1981), 1770–1773.
- Max Kollep, Georgia Konstantinou, Jorge Madrid-Wolff, Antoine Boniface, Lorenz Hagelüken, Pradeep Vallachira Warriam Sasikumar, Gurdial Blugan, Paul Delrot, Damien Loterie, Juergen Brugger, et al. 2022. Tomographic volumetric additive manufacturing of silicon oxycarbide ceramics. *Advanced Engineering Materials* 24, 7 (2022), 2101345.
- Samuli Laine, Janne Hellsten, Tero Karras, Yeongho Seol, Jaakko Lehtinen, and Timo Aila. 2020. Modular Primitives for High-Performance Differentiable Rendering. *ACM Transactions on Graphics* 39, 6 (2020).
- Chi Chung Li, Joseph Toombs, Vivek Subramanian, and Hayden K. Taylor. 2024a. Multi-beam phase mask optimization for holographic volumetric additive manufacturing. *arXiv:2401.15590 [physics.optics]*
- Chi Chung Li, Joseph Toombs, Hayden K. Taylor, and Thomas J. Wallin. 2024b. Generalized projection optimization model for tomographic volumetric additive manufacturing. In *Advanced Fabrication Technologies for Micro/Nano Optics and Photonics XVII*, Vol. 12898. SPIE, 82–92. <https://doi.org/10.1117/12.3008459>
- Tzu-Mao Li, Miika Aittala, Frédo Durand, and Jaakko Lehtinen. 2018. Differentiable monte carlo ray tracing through edge sampling. *ACM Transactions on Graphics (TOG)* 37, 6 (2018), 1–11.
- Zongling Li, Qingshu Hou, Zhipeng Wang, Fanjiao Tan, Jin Liu, and Wei Zhang. 2021. End-to-end learned single lens design using fast differentiable ray tracing. *Optics Letters* 46, 21 (2021), 5453–5456.
- Shichen Liu, Tianye Li, Weikai Chen, and Hao Li. 2019. Soft rasterizer: A differentiable renderer for image-based 3d reasoning. In *Proceedings of the IEEE/CVF international conference on computer vision*. 7708–7717.
- Damien Loterie, Paul Delrot, and Christophe Moser. 2019. Method and apparatus for volumetric additive manufacturing with digital distortion compensation. US Patent App. 17/762,834.
- Damien Loterie, Paul Delrot, and Christophe Moser. 2020. High-resolution tomographic volumetric additive manufacturing. *Nature Communications* 11, 11 (Feb. 2020), 852. <https://doi.org/10.1038/s41467-020-14630-4>
- Jorge Madrid-Wolff, Antoine Boniface, Damien Loterie, Paul Delrot, and Christophe Moser. 2022. Controlling light in scattering materials for volumetric additive manufacturing. *Advanced Science* 9, 22 (2022), 2105144.
- Jorge Madrid-Wolff, Joseph Toombs, Riccardo Rizzo, Paulina Nuñez Bernal, Dominique Porcincula, Rebecca Walton, Bin Wang, Frederik Kotz-Helmer, Yi Yang, David Kaplan, Yu Shrike Zhang, Marcy Zenobi-Wong, Robert R. McLeod, Bastian Rapp, Johanna Schwartz, Maxim Shusteff, Hayden Talyor, Riccardo Levato, and Christophe Moser. 2023. A review of materials used in tomographic volumetric additive manufacturing. *MRS Communications* 13, 5 (Oct. 2023), 764–785. <https://doi.org/10.1557/s43579-023-00447-x>
- Ben Mildenhall, Pratul P. Srinivasan, Matthew Tancik, Jonathan T. Barron, Ravi Ramamoorthi, and Ren Ng. 2020. NeRF: Representing Scenes as Neural Radiance Fields for View Synthesis. In *ECCV*.

- Thomas Müller, Alex Evans, Christoph Schied, and Alexander Keller. 2022. Instant neural graphics primitives with a multiresolution hash encoding. *ACM transactions on graphics (TOG)* 41, 4 (2022), 1–15.
- Jacob Munkberg, Jon Hasselgren, Tianshang Shen, Jun Gao, Wenzheng Chen, Alex Evans, Thomas Müller, and Sanja Fidler. 2022. Extracting Triangular 3D Models, Materials, and Lighting From Images. In *Proceedings of the IEEE/CVF Conference on Computer Vision and Pattern Recognition (CVPR)*. 8280–8290.
- F Natterer. 2001. Inversion of the attenuated Radon transform. *Inverse Problems* 17, 1 (feb 2001), 113. <https://doi.org/10.1088/0266-5611/17/1/309>
- Merlin Nimier-David, Thomas Müller, Alexander Keller, and Wenzel Jakob. 2022. Unbiased inverse volume rendering with differential trackers. *ACM Transactions on Graphics (TOG)* 41, 4 (2022), 1–20.
- Merlin Nimier-David, Sébastien Speirer, Benoît Ruiz, and Wenzel Jakob. 2020. Radiative backpropagation: An adjoint method for lightning-fast differentiable rendering. *ACM Transactions on Graphics (TOG)* 39, 4 (2020), 146–1.
- Merlin Nimier-David, Delio Vicini, Tizian Zeltner, and Wenzel Jakob. 2019. Mitsuba 2: A retargetable forward and inverse renderer. *ACM Transactions on Graphics (TOG)* 38, 6 (2019), 1–17.
- Thomas Klaus Nindel, Tomáš Iser, Tobias Rittig, Alexander Wilkie, and Jaroslav Krivánek. 2021. A gradient-based framework for 3D print appearance optimization. *ACM Trans. Graph.* 40, 4, Article 178 (jul 2021), 15 pages. <https://doi.org/10.1145/3450626.3459844>
- Jorge Nocedal. 1980. Updating quasi-Newton matrices with limited storage. *Mathematics of computation* 35, 151 (1980), 773–782.
- Jan Novák, Ilian Georgiev, Johannes Hanika, and Wojciech Jarosz. 2018. Monte Carlo Methods for Volumetric Light Transport Simulation. *Computer Graphics Forum (Proceedings of Eurographics - State of the Art Reports)* 37, 2 (May 2018).
- Jan Novák, Andrew Selle, and Wojciech Jarosz. 2014. Residual ratio tracking for estimating attenuation in participating media. *ACM Trans. Graph.* 33, 6 (2014), 179–1.
- Antony Orth, Kathleen L. Sampson, Kayley Ting, Jonathan Boisvert, and Chantal Paquet. 2021. Correcting ray distortion in tomographic additive manufacturing. *Optics Express* 29, 7 (March 2021), 11037–11054. <https://doi.org/10.1364/OE.419795>
- Antony Orth, Daniel Webber, Yujie Zhang, Kathleen L. Sampson, Hendrick W. de Haan, Thomas Lacelle, Rene Lam, Daphne Solis, Shyamaleeswari Dayanandan, Taylor Waddell, Tasha Lewis, Hayden K. Taylor, Jonathan Boisvert, and Chantal Paquet. 2023. Deconvolution volumetric additive manufacturing. *Nature Communications* 14, 11 (July 2023), 4412. <https://doi.org/10.1038/s41467-023-39886-4> 0 citations (Crossref) [2023-08-15].
- Maxine Peroni-Scharf and Szymon Rusinkiewicz. 2023. Constructing Printable Surfaces with View-Dependent Appearance. In *ACM SIGGRAPH 2023 Conference Proceedings*. 1–10.
- Charles M. Rackson, Kyle M. Champlie, Joseph T. Toombs, Erika J. Fong, Vishal Bansal, Hayden K. Taylor, Maxim Shusteff, and Robert R. McLeod. 2021. Object-space optimization of tomographic reconstructions for additive manufacturing. *Additive Manufacturing* 48 (Dec. 2021), 102367. <https://doi.org/10.1016/j.addma.2021.102367>
- Charles M. Rackson, Joseph T. Toombs, Martin P. De Beer, Caitlyn C. Cook, Maxim Shusteff, Hayden K. Taylor, and Robert R. McLeod. 2022. Latent image volumetric additive manufacturing. *Optics Letters* 47, 5 (March 2022), 1279–1282. <https://doi.org/10.1364/OL.449220>
- Pengfei Shen, Ruizeng Li, Beibei Wang, and Ligang Liu. 2023. Scratch-based Reflection Art via Differentiable Rendering. *ACM Trans. Graph.* 42, 4, Article 65 (jul 2023), 12 pages. <https://doi.org/10.1145/3592142>
- Zheng Shi, Ilya Chugunov, Marin Bijelic, Geoffroi Côté, Jiwoo Yeom, Qiang Fu, Hadi Amata, Wolfgang Heidrich, and Felix Heide. 2024. Split-Aperture 2-in-1 Computational Cameras. *ACM Transactions on Graphics (TOG)* 43, 4 (2024), 1–19.
- Denis Sumin, Tobias Rittig, Vahid Babaei, Thomas Nindel, Alexander Wilkie, Piotr Didyk, Bernd Bickel, J KRivánek, Karol Myszkowski, and Tim Weyrich. 2019. Geometry-aware scattering compensation for 3D printing. *ACM Transactions on Graphics* 38, 4 (2019).
- Qilin Sun, Congli Wang, Fu Qiang, Dun Xiong, and Heidrich Wolfgang. 2021. End-to-end complex lens design with differentiable ray tracing. *ACM Trans. Graph.* 40, 4 (2021), 1–13.
- Arjun Teh, Matthew O'Toole, and Ioannis Gkioulekas. 2022. Adjoint nonlinear ray tracing. *ACM Trans. Graph.* 41, 4, Article 126 (jul 2022), 13 pages. <https://doi.org/10.1145/3528223.3530077>
- Kenji Tojo, Ariel Shamir, Bernd Bickel, and Nobuyuki Umetani. 2023. Stealth Shaper: Reflectivity Optimization as Surface Stylization. In *ACM SIGGRAPH 2023 Conference Proceedings*. 1–10.
- Joseph Toombs, Chi Chung Li, and Hayden Taylor. 2024. Roll-to-roll tomographic volumetric additive manufacturing for continuous production of microstructures on long flexible substrates. [arXiv:2402.10955 \[physics.app-ph\]](https://arxiv.org/abs/2402.10955)
- Joseph T. Toombs, Manuel Lutz, Caitlyn C. Cook, Sophie Jenne, Chi Chung Li, Bastian E. Rapp, Frederik Kotz-Helmer, and Hayden K. Taylor. 2022. Volumetric additive manufacturing of silica glass with microscale computed axial lithography. *Science* 376, 6590 (April 2022), 308–312. <https://doi.org/10.1126/science.abm6459>
- John R Tumbleston, David Shirvanyants, Nikita Ermoshkin, Rima Janusziewicz, Ashley R Johnson, David Kelly, Kai Chen, Robert Pinschmidt, Jason P Rolland, Alexander Ermoshkin, et al. 2015. Continuous liquid interface production of 3D objects. *Science* 347, 6228 (2015), 1349–1352.
- Eric Veach. 1998. *Robust Monte Carlo methods for light transport simulation*. Stanford University.
- Delio Vicini, Sébastien Speirer, and Wenzel Jakob. 2021. Path replay backpropagation: Differentiating light paths using constant memory and linear time. *ACM Transactions on Graphics (TOG)* 40, 4 (2021), 1–14.
- Daniel Webber, Yujie Zhang, Michel Picard, Jonathan Boisvert, Chantal Paquet, and Antony Orth. 2023a. Versatile volumetric additive manufacturing with 3D ray tracing. *Optics Express* 31, 4 (Feb. 2023), 5531–5546. <https://doi.org/10.1364/OE.481318>
- Daniel Webber, Yujie Zhang, Michel Picard, Jonathan Boisvert, Chantal Paquet, and Antony Orth. 2023b. Versatile volumetric additive manufacturing with 3D ray tracing. *Optics Express* 31, 4 (2023), 5531–5546.
- Daniel Webber, Yujie Zhang, Kathleen L. Sampson, Thomas Lacelle, Chantal Paquet, Jonathan Boisvert, and Antony Orth. 2024. Micro-optics fabrication using blurred tomography. [arXiv:2401.08799 \[physics.optics\]](https://arxiv.org/abs/2401.08799)
- Felix Wechsler, Carlo Gigli, Jorge Madrid-Wolff, and Christophe Moser. 2024. Wave optical model for tomographic volumetric additive manufacturing. *Optics Express* 32, 8 (April 2024), 14705–14712. <https://doi.org/10.1364/OE.521322>
- Todd H Weisgraber, Martin P de Beer, Sijia Huang, John J Karnes, Caitlyn C Cook, and Maxim Shusteff. 2023. Virtual Volumetric Additive Manufacturing (VirtualVAM). *Advanced Materials Technologies* 8, 23 (2023), 2301054.
- E Woodcock, T Murphy, P Hemmings, and S Longworth. 1965. Techniques used in the GEM code for Monte Carlo neutronics calculations in reactors and other systems of complex geometry. In *Proc. Conf. Applications of Computing Methods to Reactor Problems*, Vol. 557. Argonne National Laboratory.
- Kang Wu, Renjie Chen, Xiao-Ming Fu, and Ligang Liu. 2022. Computational mirror cup and saucer art. *ACM Transactions on Graphics (TOG)* 41, 5 (2022), 1–15.
- Tizian Zeltner, Ilian Georgiev, and Wenzel Jakob. 2020. Specular manifold sampling for rendering high-frequency caustics and glints. *ACM Trans. Graph.* 39, 4, Article 149 (aug 2020), 15 pages.
- Cheng Zhang, Bailey Miller, Kai Yan, Ioannis Gkioulekas, and Shuang Zhao. 2020. Path-Space Differentiable Rendering. *ACM Trans. Graph.* 39, 4 (2020), 143:1–143:19.

A MATERIALS AND METHODS

A.1 Optical Setup

We show a simplified schematic of our optical setup in Figure 2a, and provide more detail about it here. Blue light illumination with $\lambda = 405$ nm (HL40033G, Ushio, Japan) was guided through a square multimode optical fibre (WF 70×70/115/200/400N, CeramOptec, Germany) onto the DMD (VIS-7001, Vialux, Germany). The light of the blue laser diodes can be assumed to be very homogeneous and square shaped after the fiber output.

The maximum continuous power of the light source is 265 mW in the printing plane. A 4f system consisting of two lenses with 150 mm (LA4874-A-ML, Thorlabs, USA) and 150 mm (AC508-150-A-ML, Thorlabs, USA) (with an iris aperture at the Fourier stop to filter out higher diffraction orders) images the DMD onto the center of the glass vial. The light is collimated within the depth of field, which is set to be roughly equal to the vial diameter. The depth of field is directly correlated to the size of an aperture, which we can control, and set to be roughly equal to the vial diameter. Hence, we can model this as a directional area light (i.e. light is only emitted along the normal direction). In the printing plane, one DMD pixel has an area of $13.79 \times 13.79 \mu\text{m}^2$, which corresponds to a total illuminated area of $7.06 \times 7.06 \text{ mm}^2$ for a pattern resolution of 512^2 pixels.

A.2 Vials

We use cylindrical vials (Flachbodengläser, made of AR-Glas, $n = 1.514$) whose diameters are $D_{\text{inner}} = (15.33 \pm 0.08) \text{ mm}$ and $D_{\text{outer}} = (16.77 \pm 0.08) \text{ mm}$. We mount them on a high-precision rotary stage (X-RSW60C, Zaber, Canada).

Table 3. Printing parameters for different experiments. It shows the resin with the respective concentration of TPO and TiO_2 . Further, the measured absorption coefficient μ_a and extinction coefficient μ_t . Also the total laser exposure time and the electrical current of the two laser diodes each is noted.

ID	m_{resin} in g	m_{TPO} in mg	m_{TiO_2} in mg	μ_a in mm^{-1}	μ_t in mm^{-1}	exposure time in s	laser diode current in mA
#1	71.19	43.0	0	0.1148	0.1148	27	1090
#2	71.19	43.0	0	0.1148	0.1148	27	1042
#3	71.19	43.0	0	0.1148	0.1148	27	820
#4	65.94	47.4	0	0.1325	0.1325	36	540 + 540
#5	69.54	56.5	0	0.1462	0.1462	36	650 + 650
#6	69.54	56.5	0	0.1462	0.1462	36	645 + 645
#7	66.95	48.0	3.4	0.1299	0.3006	162	750 + 750
#8	66.95	48.0	3.4	0.1299	0.3006	36	700 + 700
#9	67.26	54.8	2.7	0.1429	0.2781	27	457 + 457
#10	67.26	54.8	2.7	0.1429	0.2781	36	700 + 700
#11	67.26	54.8	2.7	0.1429	0.2781	36	712.5 + 712.5
#12	67.26	54.8	2.7	0.1429	0.2781	36	725 + 725

The square vials we used are common spectrophotometer cuvettes ($L_{\text{outer}} = (12.43 \pm 0.03)$ mm, $L_{\text{inner}} = (10.07 \pm 0.03)$ mm, $n = 1.58$) made of polystyrene (7590 30, Brand, Germany).

A.3 Resin Preparation

For the photo-curable resins we used di-pentaerythritol pentaacrylate (SR399, Sartomer, France) which was mixed with phenylbis(2,4,6-trimethylbenzoyl) phosphine oxide (TPO, 97%; Sigma-Aldrich, USA) in a planetary mixer (KK-250SE, Kurabo, Japan). The refractive index was experimentally determined to be $n = 1.4849$. As scattering material we used TiO_2 (21 nm primary particle size (TEM), $\geq 99.5\%$ trace metals basis, Sigma-Aldrich). TPO and TiO_2 were first diluted in isopropanol before mixing with the resin.

A.4 Postprocessing of printed parts

The postprocessing critically affects the final print. After the print, we pour the object into a vial containing the solvent Propylenglycolmonomethyletheracetat (PGMEA, Sigma-Aldrich, USA). This vial was then gently shaken with a Stuart Microtitre plate shaker SSM5 or a Reagenzglassschüttler Genie Vortex Mixer Modell Vortex-Genie 2. After 25 minutes of shaking we usually replaced the old solvent with a new one and shake for another 25 minutes. Then, we would add a significant amount of fresh TPO solved in Isopropanol to the object after we removed the PGMEA. The whole vial was cured under a high power UV lamp for some minutes. After UV curing we would remove the remaining solvent mixture with a pipette, pour the object on a microscopy slide and let the object dry under the UV lamp again.

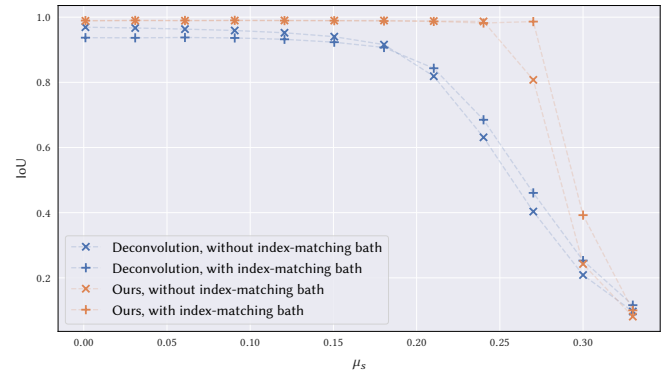


Fig. 15. We compare the results from the experiment in Figure 12, with and without an index-matching bath. The plot shows that the previous observations continue to hold in this configuration.